Cement and Concrete Composites 166 (2026) 106379

Contents lists available at ScienceDirect

Cement and Concrete Composites

journal homepage: www.elsevier.com/locate/cemconcomp

A numerical framework for fibre orientation prediction in fibre-reinforced concrete tunnel linings

Giacomo Rizzieri [a],*, Andrea Marcucci [a], Stefano Guanziroli [b], Massimiliano Cremonesi [a], Liberato Ferrara [a]

[a] Department of Civil and Environmental Engineering, Politecnico di Milano, Piazza Leonardo da Vinci, 32, Milano, 20133, Italy
[b] Hinfra Ltd, Via Luigi Buzzi, 6, Casale Monferrato, 15033, Italy

ARTICLE INFO

Keywords:
Fibre-reinforced self-compacting concrete (FR-SCC)
Rheology
Particle finite element method (PFEM)
Slip-forming tunnel linings
Fibre orientation factor

ABSTRACT

The use of Fibre-Reinforced Self-Compacting Concrete (FR-SCC) has increased significantly in recent decades, due to its superior flowability, workability, and enhanced mechanical performances. These characteristics have made it particularly suitable for both cast-in-place and precast applications, ranging from slabs to tunnel segments. One of the main advantages of FR-SCC is the possibility to control fibre dispersion, which directly influences the material's structural performance. However, evaluating fibre dispersion within the targeted elements remains a significant challenge, as it depends on both the rheological properties of the mix and the casting process. Structural codes require to account for fibre orientation in the design phase through the definition of an orientation factor. For complex applications, such as the casting of the FR-SCC tunnel lining considered in this study, determining this factor in advance is particularly challenging. To address this issue, a simple yet effective framework for predicting fibre orientation in arbitrary casting processes is proposed. A fluid FEM-based numerical model is employed to accurately compute flow lines during casting. A time-dependent Bingham law is used to reproduce the FR-SCC rheological behaviour, while calibrating the parameters, to account for the effect of fibres, by means of ICAR rheometer tests. Based on the numerically computed velocity field during casting, a novel definition of the orientation factor is introduced. The approach is validated through comparison with experimental results obtained from a non-destructive magnetic survey of the fibre dispersion, performed on full-scale mock-ups of FR-SCC tunnel linings.

1. Introduction

In recent years, the field of concrete construction has witnessed groundbreaking advances, among which several are linked to the better control over the fresh state, i.e., that phase occurring immediately after mixing and before setting. As a matter of fact, the fresh state properties not only play a pivotal role in determining the durability, strength, and overall performance of the hardened concrete structures [1], but also have a central role in the development of advanced construction materials and technologies.

In the last decades, Self-Compacting Concrete (SCC) has been developed and popularized to solve, among the others, casting problems in structural elements with highly congested reinforcement. SCC is in fact characterized by high flowability, allowing the possibility to fill intricate forms and heavily reinforced details without mechanical vibration. This innovation, while simplifying the construction process, has also resulted into a better overall quality of the finished structures, from aesthetics to mechanical performance and durability. These superior outcomes are primarily attributed to the unique mix design required to achieve enhanced performances in the fresh state.

These performances can be better quantified under the commonly employed assumption that fresh concrete behaves as a homogeneous Bingham fluid. Specifically, SCC is characterized by yield stress values that are sufficiently low to guarantee the ability to flow under its own weight, but high enough to prevent particle segregation under static conditions [2]. Additionally, moderate values of plastic viscosity help to maintain a uniform distribution of particle suspension during curing.

The slump test is the most common experimental method for evaluating the workability and the Bingham parameters of standard fresh concrete in practice. The yield stress can be estimated using analytical formulas [3,4] that correlate it with the measured height loss. In the case of SCC, its high flowability necessitates using the spread diameter at the end of self-weight-driven flow to estimate yield stress

* Corresponding author.
E-mail addresses: giacomo.rizzieri@polimi.it (G. Rizzieri), andrea.marcucci@polimi.it (A. Marcucci), stefano.guanziroli@hinfra.it (S. Guanziroli), massimiliano.cremonesi@polimi.it (M. Cremonesi), liberato.ferrara@polimi.it (L. Ferrara).

https://doi.org/10.1016/j.cemconcomp.2025.106379
Received 13 January 2025; Received in revised form 16 September 2025; Accepted 18 October 2025
Available online 24 October 2025

via analytical formulations. Additionally, the time to reach a 500 mm spread or flow cessation [5] serves as an indicator of plastic viscosity and dynamic resistance to segregation. Other tests like the V-funnel and L-box provide additional insights into specific SCC properties [6]. The V-funnel measures flowability and viscosity by timing the material's passage through a narrow funnel, while the L-box evaluates the ability of SCC to flow around obstacles without segregation. For a more detailed rheological assessment, however, rheometer tests are essential [7].

Rotational rheometers, through the measure of the rotational speed and torque, can provide a complete and accurate evaluation of the rheological parameters of the Bingham's model [8] or of its power-law variations [9]. Moreover, rheometers can asses the material flow curve, highlighting nonlinear phenomena like shear-thinning and shear-thickening or time-dependent reversible effects, i.e, thixotropy [10]. A recent review of the types of rheometers commercially available and their functioning is reported in [11].

Combining the SCC technology with that of Fibre-Reinforced Concrete (FRC), the so-called Fibre-Reinforced Self-Compacting Concrete (FR-SCC) is obtained. The use of FR-SCC offers significant benefits with respect to standard FRC, such as improved fibre dispersion preventing downward settlement, enhanced fibre-matrix bond, and greater durability due to the high compactness of the SCC matrix [12]. Additionally, as reported in [13] this synergy enables to obtain a uniform distribution of fibres within the cast elements, or alternatively, to align fibres along preferential directions by means of a tailored casting process.

This is an important point, since fibres distribution and orientation can greatly affect the toughness of the hardened material [14] and hence the overall performance of the intended FR-SCC structural application. The *fib* Model Code 2010 [15] and the recently issued *fib* Model Code 2020 [16] provide prescriptions and recommendations for the identification of suitable post-craking constitutive law representative of the true crack bridging effect exerted from fibres. In particular, they recommend to scale the post-cracking relationship based on an orientation factor, which accounts for fibre orientation with respect to the direction of the principal (tensile) stress [17]. However, the structural codes do not prescribe a specific way on how to compute the orientation factor, which instead requires to be experimentally quantified with reference to each specific case [18]. In a recent study [19], possible definitions for the orientation factor in 2D and 3D, as well as practical methods for assessing fibre orientation, were reviewed.

Destructive methods are straightforward and can rely either on direct manual counting of the fibres on the fracture surface [20,21] in case of low fibres dosages, or on image analysis [13,22] and X-ray imaging [20] for higher fibres dosages and if quantitative information on fibre orientations are required. Various non-destructive techniques have also been developed for monitoring fibre dispersion, including impedance spectroscopy with alternating current [14,23], magnetic surveys [18,24], and computed axial tomography scanning [25].

In all these cases fibre distributions can only be assessed *a posteriori*. A simplified semi-empirical relation allowing for the prediction of the average orientation factor in a section as a function of the rheological behaviour, the length of the fibres and the geometry of the element to be cast has been proposed in [26]. Alternatively, numerical simulations tools for fresh concrete flow [27] can be extended to account for the presence of fibres.

In the pioneering work by Folgar and Tucker [28] a mathematical model was introduced describing the fibre orientation state in form of a probability density function. The model was later modified in [29], introducing an orientation tensor and its evolution equation, accounting for transport (by the flow) and diffusion (due to fibres interaction). Even though the computational cost of these approaches is non-negligible, they can efficiently predict fibre orientation when coupled with FEM [30] or particle-based methods [31]. A different approach, acceptable if the fibres concentration is moderately low, would be to assume fibres aligned with the flow curves [26]. This strategy was validated for example in [32,33], where a Lagrangian FEM model was exploited to determine fibre orientation during casting of simple beams and slabs.

All the methods discussed above rely on a one-way coupling assumption, i.e., fibre orientations are influenced by the flow, but not the contrary. A more realistic representation of the casting process, can be done by materializing the fibres in the simulation. Some examples of two-way coupling simulations based on this approach are [34], relying on the discrete element method, or [35], where the fluid part was treated with CFD techniques, while fibres were modelled as immersed rigid objects.

The aim of this work is to present a simple yet effective procedure for predicting the orientation factor, required for structural design calculations in accordance with the fib Model Code 2010 [15] and 2020 [16], in the context of complex casting processes. Rather than relying on time-consuming manual measurements, an approach based on an advanced, in-house developed numerical tool, calibrated using rheological test data, is proposed. The objective is to enable rapid estimation of the orientation factor even for complex geometries and full-scale engineering applications, where experimental measurement is often impractical due to size and geometric constraints. Specifically, the study focuses on the work conducted by the Italian company Hinfra Ltd, which is developing the Extruded Tunnel Lining Regeneration (ETLR) technology for refurbishing existing tunnel linings [36]. This technology involves segmental extrusion of steel FR-SCC tunnel linings using a horizontal automated slip-forming process, offering a more efficient approach to tunnel refurbishment compared to traditional methods.

The work focuses on the following original aspects:

1. ICAR rheometer measurements were conducted following a custom-developed protocol to assess the effect of fibres on the rheological properties of the cementitious mix. Additionally, the role of fibres in influencing both reversible (thixotropic) and irreversible structuration phenomena was also established.
2. A Particle Finite Element Method (PFEM) [37,38] model of the casting process of the tunnel lining mock-ups was developed, incorporating a time-dependent Bingham law to describe the material behaviour. The parameters for this model were calibrated using the rheometer test data, enabling the accurate computation of the flow lines during mould filling. Given the relatively low fibre volume content (approximately 0.5%) in the matrix of the FR-SCC used in the casting process, the material can be considered to be in the diluted regime [39]. This supports the adoption of a one-way coupling approach, where fibres are assumed to align with the flow streamlines.
3. A straightforward yet effective method for computing the orientation factor, based only on the knowledge of the velocity field during casting, is proposed. Its generality ensures applicability with any numerical tool capable of generating the flow lines for the casting process.
4. A non-destructive survey campaign, by means of a magnetic-inductance based method, was performed on the four full-scale slip-formed mock-ups to evaluate the actual fibre distribution within/inside the structures, as built. Comparisons between the experimental results and the numerical predictions demonstrated good agreement, validating the developed framework and confirming its applicability to different case studies.

The paper is organized as follows. In Section 2 the composition of the employed cementitious mixes is given, the rotational rheometer tests are described and the results in terms of the identified Bingham rheological properties and their time-evolution are reported and commented. In Section 3 the FEM numerical model is concisely presented, focusing on the geometry of the problem, the casting process and the inclusion of the time-dependent effects. Section 4 firstly reports

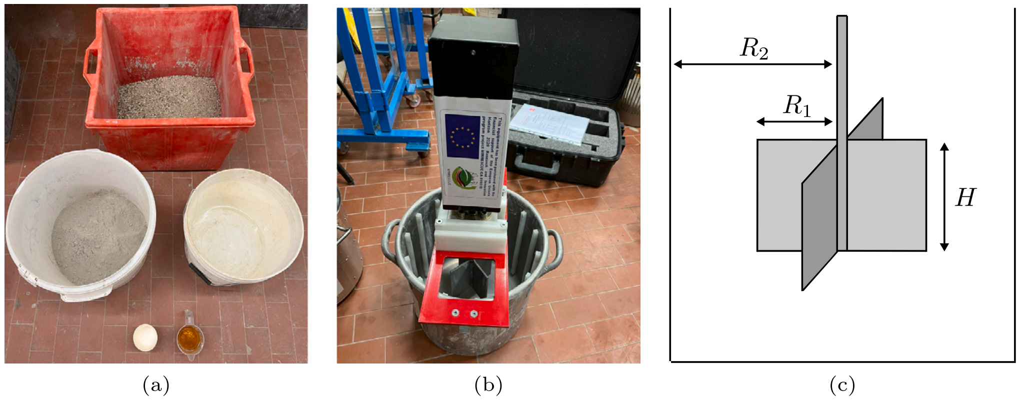

Fig. 1. Mix M1 composition (a), ICAR rheometer (b) and vane and container of the ICAR rheometer geometry (c).

the simulation results, including the representation of the flow line at different time instants. Successively, it details the proposed procedure to evaluate the orientation factor and computes it on thirteen relevant sections of each of the investigated full scale mock-ups. Finally, the numerical results, in terms of fibre orientations, are compared to those obtained from the magnetic survey on the full scale mock-ups, validating the overall procedure.

2. Materials and methods

2.1. Cementitious mix compositions and ICAR rheometer

The two mixes considered in this work, developed by Hinfra Ltd specifically for the ETLS project, are both SCC mixes, characterized by the constituents represented in Fig. 1-a and the relative proportions reported in Table 1. The second mix (M2), differs from the first one (M1) due to the presence of Dramix®3D steel fibres, of 60 mm length and 0.9 mm diameter, thus resulting in an aspect ratio $r = 66.7$. The fibre volume content is $\phi_f \simeq 0.5\%$, thus according to [39], the fibre factor, which is defined as $\phi_f \cdot r \simeq 0.34$ is by far lower than the upper limit for the diluted regime, indicating that the influence of the fibres on the rheological behaviour of the cementitious material is low.

Table 1
Cementitious mixes compositions.

Component	Mix M1	Mix M2
Binder	600 kg/m^3	600 kg/m^3
Water	210 kg/m^3	210 kg/m^3
Aggregates	1400 kg/m^3	1400 kg/m^3
Superplasticizer	11.7 kg/m^3	11.7 kg/m^3
Steel fibres	–	40 kg/m^3

For each mix, the constituents were weighted to respect the proportions indicated in Table 1 and then gradually added in a concrete mixer. First, the powder components were mixed, after which the water and superplasticizer were added simultaneously. In case of mix M2, steel fibre reinforcement were added only at the end, and mixed for a couple of minutes. Specific details about the binder composition and mixing procedure are omitted due to patent protection. Once the mix was ready it was poured in the ICAR rotational rheometer. The ICAR rheometer [40], represented in Fig. 1-b, is a portable instrument composed of a cylindrical container and a motorized vane, whose dimensions are reported in Fig. 1-c.

2.2. Rheometer protocol

Two different test are generally performed with a rotational rheometer: the stress growth test and the flow curve test [40]. In the stress growth test the vane is generally rotated at a constant speed of 0.025 rps. The maximum torque measured during the test is used to calculate the static yield stress with the formula [40]:

$$\tau_0 = \frac{2T}{\pi (2R_1)^3 \left(\frac{H}{2R_1} + \frac{1}{3} \right)}, \tag{1}$$

where T is the maximum recorded torque during the test and R_1 and H are respectively the radius and the height of the vane, as shown in Fig. 1-c.

The flow curve test is used instead to determine the dynamic yield stress and the plastic viscosity. It begins with a "breakdown" period in which the vane is rotated at maximum speed to provide a consistent shearing history before measuring. The vane speed is then decreased to zero through a specified number of discrete steps. During each step, the speed is held constant and the average torque is recorded. Plotting the torque (T) versus the vane rotational speed (ω) gives the T-ω flow curve. Notice that the rotational speed is measured in rotations per second (rps). Analytical relationships have been developed to correlate the T-ω flow curve to a corresponding shear rate-shear stress law. If the T-ω curve is linear, i.e., the material follows the Bingham model, the Reiner-Riwlin equations [41] can be exploited for this task:

$$\tau_0 = \frac{\left(\frac{1}{R_1^2} - \frac{1}{R_2^2} \right)}{\ln \left(\frac{R_2}{R_1} \right) 4\pi H} T_0, \tag{2}$$

$$\mu = \frac{\left(\frac{1}{R_1^2} - \frac{1}{R_2^2} \right)}{4\pi H} G, \tag{3}$$

where T_0 and G are respectively the intercept with the T-axis and the slope of the fitted line in the T-ω graph, and R_2 is the outer container radius. Some tailored extensions for the Herschel–Bulkley and the modified Bingham law have also been proposed in [42] to deal with cement pastes showing moderate shear thinning or thickening.

The protocol employed in this study consists of periodically alternating along the selected measuring time frame the stress growth and the flow curve tests, as shown in Fig. 2. The protocol was initiated ∼10 min after the contact of the binder with the water. These initial 10 min were allocated for the mixing and the pouring of the material from the mixer into the rheometer. Alternating the two tests in time provided indications on the evolution of the rheological parameters due to structuration effects [43], either reversible (thixotropy) or irreversible (early-age hydration). The protocol was then terminated at 30 min, since the measured torque became excessively high, with the risk of damaging the rheometer.

Each constant stress growth test lasted 4 min and was conducted at the minimum rheometer velocity of 0.01 rps in order to allow the material to structure. In the flow curve test the initial breakdown period was instead replaced with a step-wise increase of the rotational

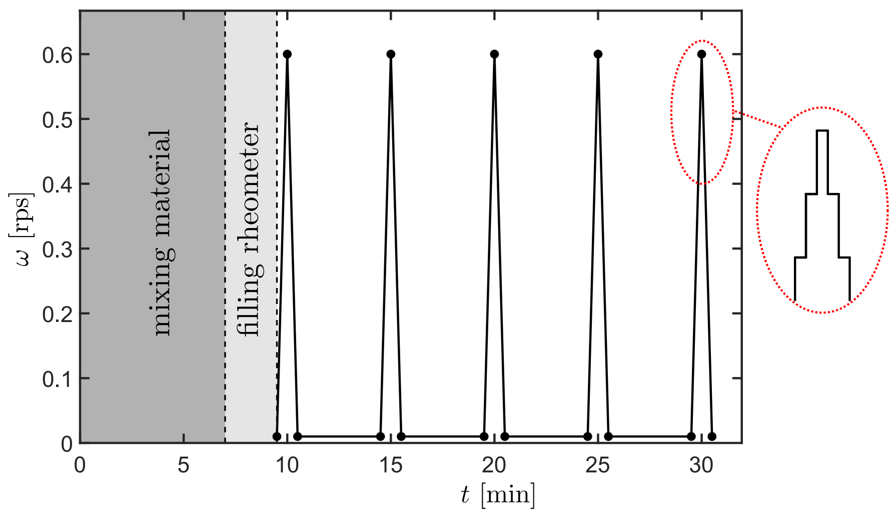

Fig. 2. Adopted rheometer protocol, consisting of alternating a modified (ramp-up and ramp-down) flow curve test and a stress growth test.

speed (ramp-up phase), symmetric to the step-wise descent (ramp-down phase). The ramp-up was composed of five velocity steps of the duration of 5 s each: 0.01–0.128–0.246–0.364–0.482–0.6 rps. The ramp-down five velocity steps, again of the duration of 5 s each, were inverted: 0.6–0.482–0.364–0.246–0.128–0.01 rps. At the end of the ramp-up, a consistent shear history was obtained, with the advantage that a ramp-up flow curve was also generated. As it will be detailed in the following, by post-processing operations on the ramp-up and ramp-down curves, it is possible to quantify reversible and irreversible structuration effects.

2.3. Rheometer results

Firstly, the results from the flow curve tests, in terms of the T-ω flow curves obtained at times 10–15–20–25–30 min for both mix M1 (without fibres) and mix M2 (with fibres) are reported in Fig. 3.

Regarding mix M1 (dashed lines in Fig. 3), it is observed that the ramp-up curves exhibit a slight shear-thinning thixotropic behaviour, which tends to become more evident in time. On the contrary, the ramp-down curves are substantially linear and remain so throughout the time frame of investigation, i.e. up until 30 min. This fact suggest that the structuration is almost exclusively reversible, since the ramp-up protocol is always sufficient to break the developed internal microstructure.

Looking at mix M2 results (continuous lines in Fig. 3) it clearly appears that fibres are playing a non-negligible role on the fresh state performance and its evolution over time. In particular, the ramp-up flow curves show a very marked non-linear shear-thinning behaviour, which can be explained with a reasoning on fibre orientations. In the initial steps of the ramp-up, fibres are randomly oriented, thus creating a relevant opposition to the motion. Instead, for higher rotational velocities the fibres start to align with the flow, creating less resistance and thus decreasing the mix viscosity.

To quantify thixotropic effects (i.e., fully reversible structuration [44]), the area between corresponding ramp-up and ramp-down flow curves can be computed. This operation has been performed over the range of rotational velocities of 0.128–0.482 rps. The initial and final velocity values have been excluded, as they may be less reliable due to their association with transient flow conditions. Similarly, the total (reversible and irreversible) structuration is given by the areas between the ramp-up curves at the considered time and the ramp-down curve at the initial time (t = 10 min), in the same range of velocities 0.128–0.482 rps, as shown for both Mix M1 and Mix M2 in Fig. 4.

Following a similar approach to that presented in [45], by subtracting from the total structuration the reversible structuration, the irreversible one can be computed. The results summarizing all these computations are plotted in Fig. 5-a for mix M1, showing how the irreversible structuration is very limited, and starts only after the 20 min. Almost all the structuration can be attributed to reversible effects phenomena, i.e., thixotropy. Results for Mix M2 are instead presented in Fig. 5-b, showing that the total structuration has doubled with respect to mix M1. In particular, both reversible and irreversible structuration phenomena seem to be increased by the presence of fibres. According to [45,46], fibres enhance the material's microstructure, increasing yield stress and plastic viscosity. This effect is partially reversible in the early-stages fresh cement paste, but becomes irreversible as the paste hardens, locking the fibres in place.

The flow test is generally used to compute the dynamic yield stress and the viscosity. Here, it was used for two reasons: clarify the role of fibres on structuration effects and evaluate the viscosity with its time evolution. In particular, the viscosity is computed at the different times from the ramp-down flow curves with Eq. (3). Viscosity values at different times are reported in Fig. 6-a and fitted with a linear law:

$$\mu(t) = \mu_{t=10\ \text{min}} + A^{\mu}_{thix} t, \tag{4}$$

where $\mu_{t=10\ \text{min}}$ is the initial value of the viscosity and A^{μ}_{thix} is the rate of increment of the viscosity in time.

Similarly, from the stress growth tests results, the static yield stress at each time can be computed with Eq. (1). Roussel thixotropy model [2], which postulates a linear evolution in time of the static yield stress, reads:

$$\tau_0(t) = \tau_{0,t=10\ \text{min}} + A_{thix} t, \tag{5}$$

where A_{thix} is the flocculation parameter and t[min] is the time. By fitting in the least squared sense a line through the static yield stress data, it was possible to evaluate the parameters of Roussel model for both mixes (see Fig. 6-b)

The linear fitting viscosity parameters derived from the flow curve test and the Roussel's model parameters computed from the stress growth tests are reported in Table 2. The initial yield stress in both mix M1 and M2 is about τ_0 = ∼70 − 80 Pa. These are common values for SCC concretes, which need moderate yield stresses to facilitate the filling of complex frameworks.

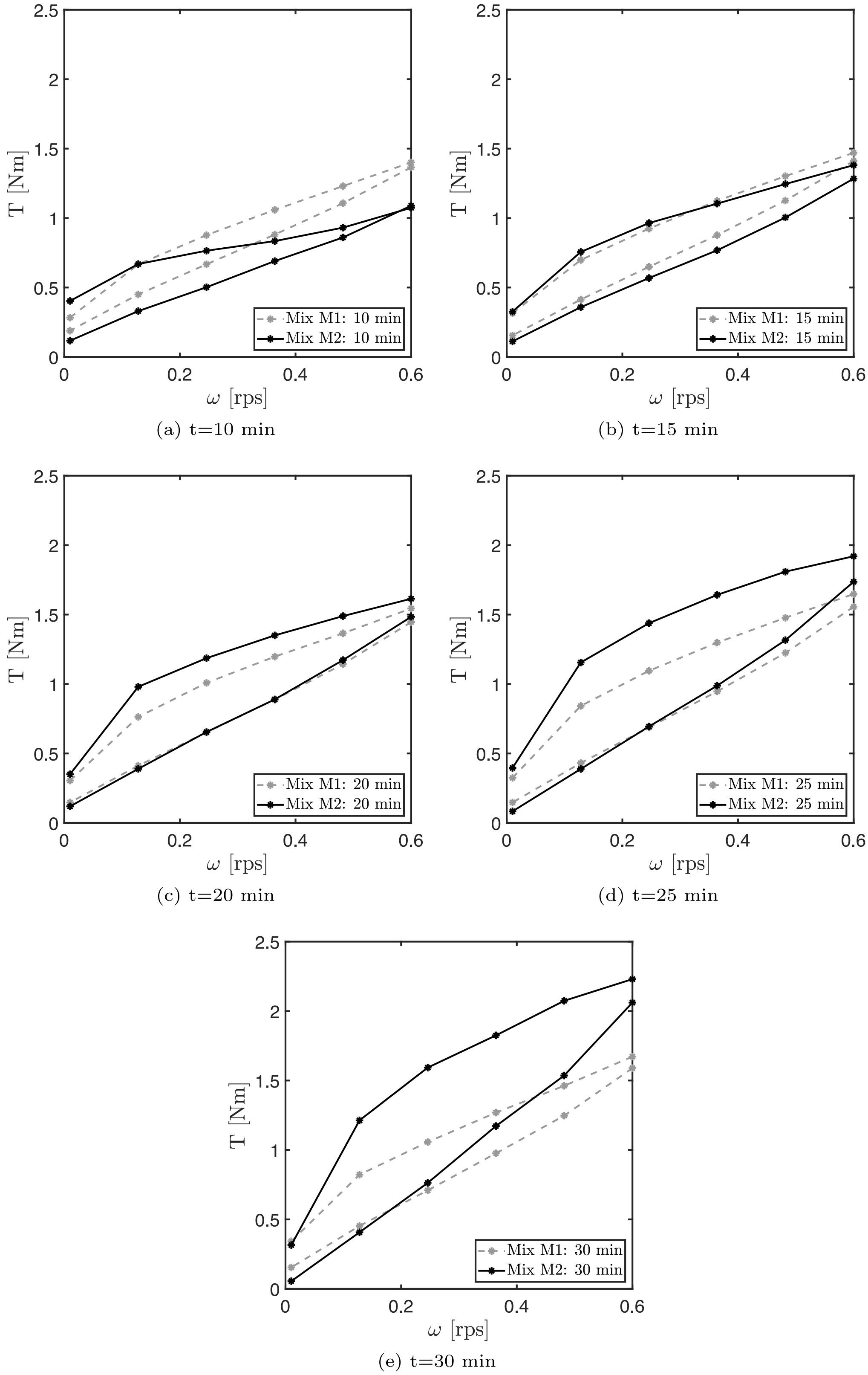

Fig. 3. Comparison between the flow curves obtained at different times $10-15-20-25-30$ min (a–e) for the M1 and M2 cementitious mixes.

Regarding the yield stress time evolution, Mix M2 is characterized by $A_{thix}^{\tau_0} = 2.91$ Pa/min, which is much larger than in Mix M1 $A_{thix}^{\tau_0} = 0.45$ Pa/min. This result is also in agreement with other studies in the literature [7,26] showing how fibres can favour re-flocculation and thus accelerate thixotropic phenomena. Additionally, the presence of fibres increases the percentage of irreversible structuration with respect to the total structuration, from ∼22% in mix M1 to ∼34% in mix M2. This phenomenon, also observed in [47], can be attributed to the dual role of

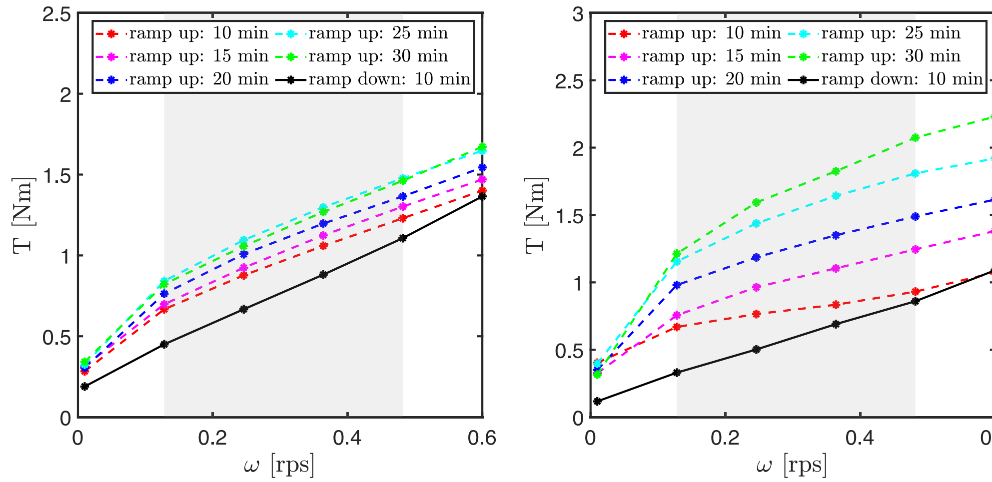

(a) (b)

Fig. 4. Ramp-up flow curves and initial (t = 10 min) ramp-down flow curve for Mix M1 (a) and Mix M2 (b). The indication of the relevant velocity range to be considered for computing structuration effects is also reported.

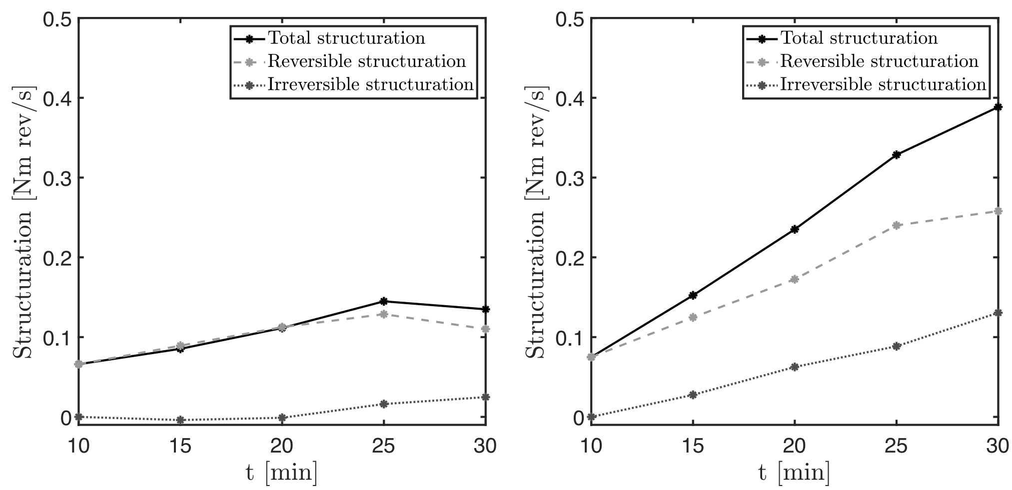

(a) t=10 min (b) t=15 min

Fig. 5. Structuration of Mix M1 without fibres (a) and Mix M2 with fibres, along a time span of 20 min.

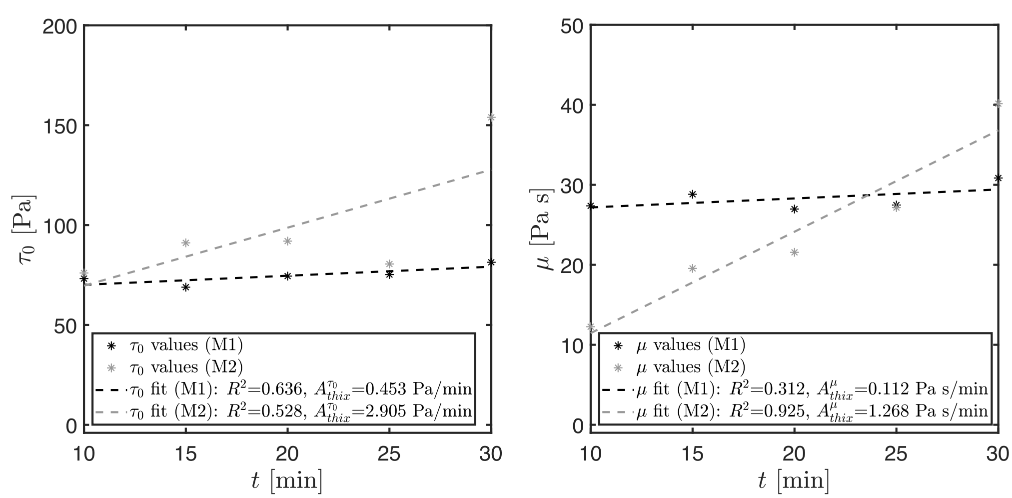

(a) t=10 min (b) t=15 min

Fig. 6. Time evolution for both mix M1 and M2 of the static yield stress (a) and of the Newtonian viscosity (b).

Table 2
Comparison between the rheological quantities and their time evolution for the two cementitious mixes.

Mix	$\tau_{0,t=10\ \mathrm{min}}$	$\mu_{t=10\ \mathrm{min}}$	$A^{\tau_0}_{thix}$	A^{μ}_{thix}	$\frac{Irr_{struct}}{Tot_{struct}} \cdot 100$
M1 (SCC)	73.22 Pa	27.87 Pa s	0.45 Pa/min	0.11 Pa s/min	21.94%
M2 (SCC+fibres)	76.02 Pa	12.26 Pa s	2.91 Pa/min	1.27 Pa s/min	33.59%

fibres: directly contributing to the microstructure and indirectly aiding in partially protecting and preserving the bonds between particles from external shearing forces.

Regarding the viscosity, in mix M1 it remains almost constant in time and approximatively of 28 Pa s, while in Mix M2 it starts from an initial value of 12.26 Pa s and successively moderately increases over time.

3. Numerical model

3.1. Governing equations and FEM discretization

The numerical method employed in this work relies on the framework developed in [48] for the simulation of standard fresh concrete tests and in [49–51] for the modelling of advanced manufacturing processes with cementitious materials. The underlying assumption is that fresh concrete can be considered as a viscous homogeneous fluid and thus its motion is governed by the Navier–Stokes equations.

Considering an evolving fluid domain Ω_t in a time interval $[0, T]$, let us denote with $\mathbf{x}$ the position vectors at time t in the local “or current” configuration. The momentum balance and mass continuity equations for an weakly compressible fluid, written for a Lagrangian observer read:

$$\rho \frac{d\boldsymbol{u}}{dt} = \nabla_{\boldsymbol{x}} \cdot \boldsymbol{\sigma} + \rho \boldsymbol{b} \quad \text{in } \Omega_t \times [0, T], \tag{6}$$

$$\frac{dp}{dt} + K \nabla_{\boldsymbol{x}} \cdot \boldsymbol{u} = 0 \quad \text{in } \Omega_t \times [0, T], \tag{7}$$

where ρ is the constant density of the fluid, $\boldsymbol{\sigma} = \boldsymbol{\sigma}(\boldsymbol{x}, t)$ is the Cauchy stress tensor, $\boldsymbol{b}$ is the vector of the body forces, $\boldsymbol{u} = \boldsymbol{u}(\boldsymbol{x}, t)$ is the velocity field, $p = p(\boldsymbol{x}, t)$ is the pressure field and K is the bulk modulus of the material. The bulk modulus K can be estimated using the relation $K = \rho c^2$, where c is the speed of sound in the material. For fresh concrete, according to [52], $c \approx 200$–$500\,\mathrm{m/s}$. For the composite material considered in this study, with a density of $\rho = 2261.7\,\mathrm{kg/m^3}$, this yields bulk modulus values in the range $K = 9.1 \times 10^7$–5.7×10^8 Pa, which are characteristic of a weakly-compressible fluid. A suitable set of initial and boundary conditions must also be prescribed for the problem to be well-posed.

In fluid dynamics it is convenient to decompose the Cauchy stress tensor in a volumetric and a deviatoric part:

$$\boldsymbol{\sigma} = -p\boldsymbol{I} + \boldsymbol{\tau}, \tag{8}$$

where $\boldsymbol{I}$ is the identity tensor and $\boldsymbol{\tau}$ is the deviatoric stress tensor. The deviatoric stress tensor expression is assigned through the rheological law. For fresh concrete, the most adopted rheological law is the Bingham model which accounts for the presence of a yield stress in the material: if the stresses are lower than the yield stress the fluid behaves as a rigid body, while, if the yield stress threshold is overcome, the fluid starts to flow. The Bingham model reads:

$$\boldsymbol{\tau}(\boldsymbol{u}) = 2\mu \epsilon(\boldsymbol{u}) + \tau_0 \frac{\epsilon(\boldsymbol{u})}{\|\epsilon(\boldsymbol{u})\|} \qquad \text{if } \|\boldsymbol{\tau}\| > \tau_0, \tag{9}$$

$$\epsilon(\boldsymbol{u}) = \boldsymbol{0} \qquad \text{otherwise}, \tag{10}$$

where μ is the fluid viscosity, τ_0 is the yield stress, $\|\bullet\|$ is the Von Mises norm and $\epsilon(\boldsymbol{u})$ is the deviatoric strain rate tensor. Due to the sharp transition between the flow regimes, which can complicate the numerical solution, the model implements the Papanastasiou exponential regularization of the Bingham law [53].

Furthermore, because the casting process of the tunnel lining mock-up takes place over a non-negligible time-span ($\simeq$15 min), material's ageing becomes relevant. The effect of phenomena like thixotropy and early-age hydration can be accounted for by prescribing proper time-evolution laws for the Bingham's model parameters. In particular, the viscosity $\mu = \mu(t)$ will evolve following Eq. (4), while the static yield stress $\tau_0 = \tau_0(t)$ according to Eq. (5), where t is interpreted as the material resting time. Additionally, since in practice structuration can only start when the material achieves a resting configuration, in the numerical model the time-evolution of the mechanical parameters is initiated only in the unyielded regions.

The discretization process begins by expressing the governing equations in their weak form, following a standard Galerkin formulation. The resulting integrals are then discretized leveraging the associative property of integration: domain-wide integrals are decomposed into a sum of element-wise integrals. Spatial discretization is carried out by approximating the continuous fluid domain with a finite element mesh. Within each element, the unknown pressure and velocity fields are interpolated using nodal values and polynomial shape functions; in this work, linear functions are used [54].

However, for incompressible or weakly-compressible materials, the choice of interpolation spaces for velocity and pressure is critical to avoid volumetric locking. Equal-order elements, such as linear triangles in 2D and tetrahedra in 3D, are generally inadmissible. To address this limitation and enable the use of equal-order pairs, the Pressure Stabilizing Petrov–Galerkin (PSPG) method [55] is employed. PSPG introduces a perturbation of the Galerkin weighting functions at the element level, yielding a modified, stabilized form of the mass conservation equation. The semi-discretized in space equation thus read:

$$\boldsymbol{M}_u \frac{\partial \boldsymbol{U}}{\partial t} + \boldsymbol{K}_{dev} \boldsymbol{U} = \boldsymbol{F}_{ext} + \boldsymbol{D}^T \boldsymbol{P}, \tag{11}$$

$$\frac{\boldsymbol{M}_p}{K} \frac{\partial \boldsymbol{P}}{\partial t} + \boldsymbol{D}\boldsymbol{U} + \boldsymbol{L}\boldsymbol{P} + \boldsymbol{C}\frac{d\boldsymbol{U}}{dt} = \boldsymbol{H}, \tag{12}$$

where $\boldsymbol{M}_u$ is the velocity mass matrix, $\boldsymbol{K}_{dev}$ is the deviatoric stiffness matrix, $\boldsymbol{F}_{ext}$ is the vectors of the external forces, $\boldsymbol{D}$ is the discrete divergence operator matrix, $\boldsymbol{M}_p$ is the pressure mass matrix, $\boldsymbol{L}$ is the PSPG Laplacian matrix and $\boldsymbol{C}$ and $\boldsymbol{H}$ are respectively a global matrix and vector, associated to the PSPG terms providing consistency.

At this stage, time discretization is introduced using the implicit backward Euler integration scheme. After spatial and temporal discretization, the governing equations result in a nonlinear system that is linearized and solved iteratively using Picard recursive scheme. Specifically, at a given time step t_{n+1} and iteration $k+1$, the following strongly coupled linear system, written in matrix form, must be solved:

$$\begin{bmatrix} \frac{\boldsymbol{M}^k_{u,n+1}}{\Delta t} + \boldsymbol{K}^k_{dev,n+1} & -\boldsymbol{D}^{T,k}_{n+1} \\ \boldsymbol{D}^k_{n+1} + \frac{\boldsymbol{C}^k_{n+1}}{\Delta t} & \frac{\boldsymbol{M}^k_{p,n+1}}{K\Delta t} + \boldsymbol{L}^k_{n+1} \end{bmatrix} \begin{bmatrix} \boldsymbol{U}^{k+1}_{n+1} \\ \boldsymbol{P}^{k+1}_{n+1} \end{bmatrix} = \begin{bmatrix} \boldsymbol{F}^k_{ext,n+1} + \frac{\boldsymbol{M}^k_{u,n+1}}{\Delta t} \boldsymbol{U}_n \\ \frac{\boldsymbol{M}^k_{p,n+1}}{K\Delta t} \boldsymbol{P}_n + \frac{\boldsymbol{C}^k_{n+1}}{\Delta t} \boldsymbol{U}_n + \boldsymbol{H}^k_{n+1} \end{bmatrix} \tag{13}$$

The solver has been fully implemented in an in-house software developed in Fortran to ensure high computational efficiency. The Intel® oneAPI Math Kernel Library (oneMKL) is employed to store all matrices and vectors in the Compressed Sparse Row (CSR) format and to perform fundamental linear algebra operations. Furthermore, the PARDISO solver from the MKL library is utilized for the direct solution of the linear systems.

3.2. Particle Finite Element Method (PFEM)

The FEM formulation adopted in this work is based on a Lagrangian point of view, which offers several advantages, among which the effortless tracking of free surfaces and the elimination of nonlinear convective terms in the equations of motion. However, since fresh concrete can undergo large deformations, the finite element mesh may become severely distorted during the analysis. This distortion can compromise accuracy and convergence.

To address these challenges, we adopt the Particle Finite Element Method (PFEM) [37,38], which augments the Lagrangian formulation with an efficient and robust re-meshing strategy. Initially developed for the simulation of free-surface flows and breaking waves [56], PFEM has since demonstrated remarkable versatility and has been successfully applied across various engineering domains. In particular, it has shown strong suitability for problems involving expanding domains [49,50,57], as well as for modelling fluids with complex rheological properties [48,54,58], making it especially well-suited for the present study.

At the core of PFEM lies a re-meshing procedure: whenever the mesh becomes excessively distorted, it is discarded, while preserving the nodal positions. A new mesh connectivity is then generated using an efficient algorithm such as the Delaunay triangulation [59]. Subsequently, the α-shape method [60] is applied to identify the physical boundaries and reconstruct the free surface. For a detailed description of PFEM, the reader is referred to [37,38].

While PFEM offers notable advantages, it is also subject to well-documented limitations, including inaccurate volume preservation due to remeshing and challenges in applying boundary conditions [38]. To address these issues within the specific context of this application, the casting process of the tunnel segment, two techniques inspired by [50,51] are employed:

1. **Modelling the continuous inflow at the casting inlet**: A non-zero Dirichlet boundary condition is imposed by representing the inlet as a set of Eulerian nodes. This approach enables accurate enforcement of the inflow boundary condition while preserving the inlet geometry. It constitutes a specific instance of the general method for imposing non-zero Dirichlet boundary conditions proposed in [50], which utilizes the concept of Arbitrary Lagrangian-Eulerian (ALE) inlet nodes.
2. **Enhancing the contact between the fluid and the rigid mould**: Instead of explicitly materializing the mould boundaries with a set of nodes, their influence on the flow is modelled through an equivalent boundary condition. Specifically, the positions of the fluid nodes are continuously monitored during the analysis, and whenever a node crosses one of the mould boundaries, defined by closed-form equations, a zero Dirichlet boundary condition is imposed on it. This strategy generalizes the contact method originally proposed in [50,58] for the interaction of a fluid with a rigid horizontal plane and improves mass conservation with respect to the standard way of treating rigid boundaries in PFEM [38].

3.3. Case study geometry and boundary conditions

As previously mentioned, the Italian company Hinfra Ltd has developed the ETLR technology for refurbishing existing tunnel linings [36]. This innovative process involves the segmental extrusion of steel FR-SCC linings using the horizontal automated slip-forming system represented in Fig. 7. The procedure starts by activating a moving module equipped with a scraping system that removes damaged layers from a 1-m-long segment of the existing tunnel lining. The thickness of the removed layer depends on the extent of the damage. Successively, a vault-shaped mould is positioned beneath the prepared section of the tunnel. Fresh concrete is then pumped through a network of pipes into the formwork until it is completely filled. Once the concrete achieves sufficient self-standing strength, the ETLR machine advances to the next segment, repeating the process iteratively until the entire tunnel is refurbished. Further details about this semi-continuous production process can be found in [61].

Four scaled mock-ups of the real tunnel lining were cast for testing and analysis purposes and are used as references in this study. The geometry of a section of the tunnel lining mock-up is reported in Fig. 8, highlighting the side face, intrados and extrados surfaces. Despite being symmetric, it is indicated that casting will be performed from the left side, as in happens in practice, where the left part of the mould is firstly completely filled before concrete starts to flow in the right part.

The flow rate measured in practice when filling the three-dimensional mould is of $q^{3D} = 20\ \mathrm{m^3/h}$ and it is associated to a circular opening of diameter $d = 0.125$ m and area $A = \frac{\pi d^2}{4} = 0.012\ \mathrm{m^2}$. From this data the velocity of the flow was established to be $u_f^{3D} = 0.45$ m/s and the total filling process lasts $t^{3D} = 878$ s.

For simplicity an equivalent plane strain 2D problem has been formulated and studied in this work, characterized by a linear filling opening of length $d = 0.125$ m. The velocity of the real case is preserved $u_f^{2D} = u_f^{3D} = u_f = 0.45$ m/s in order to keep unaltered the Reynolds number of the flow and thus the physics of the problem. Consequently the flow rate and the total time required to fill the mould in the equivalent 2D problem will be respectively $q^{2D} = 203.25\ \mathrm{m^2/h}$ and $t^{2D} = 87$ s.

To perform the simulations the material parameters derived by the rheometer tests and summarized in Table 2 have been used. The only difference is that the time-evolution laws are also scaled to achieve the same level of structuration of the real 3D case at the end of the reduced 2D time, i.e., $A_{thix}^{\tau_0,2D} = A_{thix}^{\tau_0,3D} \cdot t_{3D}/t_{2D} = 29$ Pa/min and $A_{thix}^{\mu,2D} = A_{thix}^{\mu,3D} \cdot t_{3D}/t_{2D} = 12.8$ Pa s/min, where $t_{3D}/t_{2D} \simeq 10$.

The continuous material inflow with designed velocity $u_f = 0.45$ m/s has been assigned in input in the PFEM framework with the boundary condition method developed in [49]. Gravity is acting downward with a constant acceleration of $g = 9.81\ \mathrm{m/s^2}$. A mesh size of $h_e = \frac{d}{10} = 0.0125$ m has been chosen and a time step of $\Delta t = 10^{-2}$ s has been adopted.

As demonstrated in Section 2, the low fibre volume content indicates a dilute suspension regime, meaning that the influence of the fibres on the rheological behaviour of the cementitious material is negligible. In this context, the fibres do not affect the flow dynamics, but are instead passively transported by the fluid. This justifies the use of a numerical method based on a one-way coupling approach and the assumption that fibres align perfectly with the local velocity streamlines [26]. This hypothesis significantly reduces computational costs, but comes with two key limitations: (1) the influence of fibres on the rheology must be characterized, and (2) fibre distribution and orientation are not direct outputs of the simulation, but must be obtained through post-processing.

The first limitation was addressed in the preceding section through an extensive campaign of rheometer testing. In particular, the effect of fibres on the material's rheological behaviour was systematically examined. This was achieved by calibrating the parameters of the Bingham model - namely, the plastic viscosity and the yield stress - and by quantifying how the presence of fibres alters their evolution over time. Such calibration allowed a more accurate representation of the material's flow characteristics, ensuring that the fibre-induced modifications to the rheology were properly captured in subsequent analyses.

Regarding the second limitation, as previously stated, it is reasonable to assume that fibres are transported by the flow. Consequently, their orientation can be inferred by post-processing the velocity field to compute the corresponding streamlines. This operation is relatively straightforward, as the velocity field is a direct output of the numerical simulation and streamlines computation is a standard, computationally inexpensive procedure, performed also by many commercial and open-source softwares.

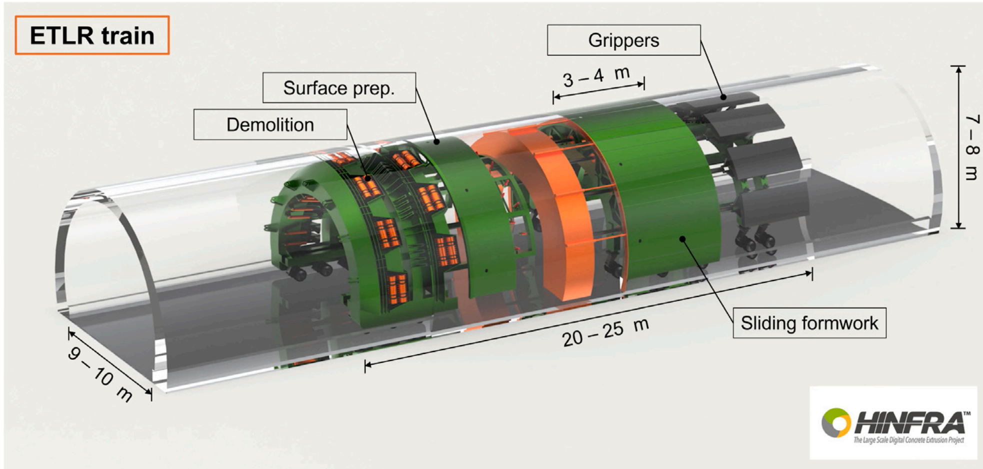

Fig. 7. Hinfra full-scale ETLR train for horizontal slip-forming of tunnel linings.

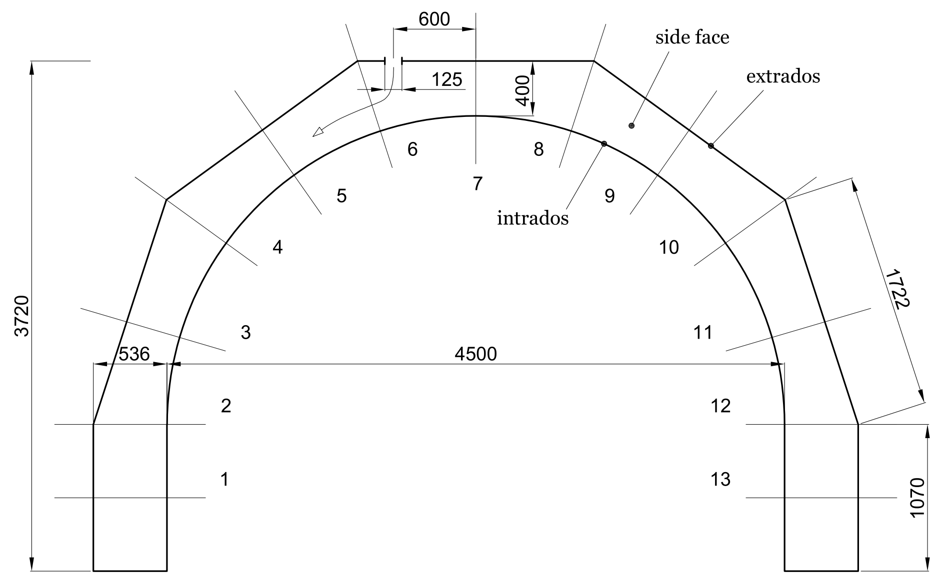

Fig. 8. 2D section of the tunnel lining mock-up, providing detailed information on the geometry (dimensions in millimetres) and boundary conditions.

4. Results

The numerical simulation of the filling of the entire mould section took only 3 to 4 h using 8 cores on a computer equipped with an Intel® Core™ i5-14600K processor (14 cores) and 32 GB of RAM. At the end of the virtual casting process the computational domain consisted of about 35 000 nodes and 70 000 triangular finite elements. The results associated to six different casting times $t = t^{2D} = 13.4$, 26.8, 40.2, 53.5, 67 and 87 s are reported in Fig. 9. In the following the 2D times are used, but it must be remembered that they are representative and can be easily converted into the actual 3D times by means of: $t^{3D} \simeq t^{2D} \cdot 10$.

The snapshots of the filling process reported in Fig. 9 also show the evolution in time of the static yield stress in the material at rest. Since the left foot of the lining is filled before the other one, the material will have more time to structurate, showcasing a difference in the static yield stress of up to 35 Pa. It is interesting to observed how on the left, a transition zone stands out below the nozzle, between the highly structured material of the left foot and the newly cast material at the end of the filling process. Even though in practice no evidence of a cold joint was observed, this local behaviour could have a repercussion on the fibres distribution. A similar trend to that shown by the static yield stress is also followed by the viscosity.

In principle, fibres are transported by the flow until the fluid velocity reduces to zero. However, once the velocity becomes zero, computing flow lines is no longer feasible, creating a challenge in evaluating fibres distribution at the end of the casting process. To address this issue, it has to be considered that as a section fills, the material's velocity in that section gradually decreases to zero. It is therefore practical to examine flow lines corresponding to a small but non-zero velocity magnitude. A threshold velocity of $u_{\mathrm{tol}} = 0.001\,\mathrm{m/s}$ has been chosen for this purpose. Typically, a particle requires approximately $T \simeq 1\,\mathrm{s}$ to decelerate from u_{tol} to zero. Assuming a linear deceleration, the particle's maximum displacement during this interval is $\Delta u = \frac{1}{2} u_{\mathrm{tol}} T = 0.0005\,\mathrm{m}$. Interpreting this displacement as the movement of the fibre's tip and assuming that the fibre rotates about its centroid, the corresponding rotation is $\Delta\theta = \frac{\Delta u}{l_f/2} \simeq 1°$, where $l_f = 60$ mm is the fibres length. This rotation is negligible for the purposes of this application, ensuring that the approximation remains valid.

The flow lines results are reported during the casting of section 2 in Fig. 10-a and of section 4 in Fig. 10-b. As already commented, flow lines associated to higher velocities are simply reproducing the transient flow during the casting process, indicating how fibres are

Fig. 9. Static yield stress distribution at different times (a–f) of the 2D process of filling of the mould.

oriented during the filling phase. Differently, flow lines associated to smaller velocities, of the order of the threshold velocity u_{tol} (darker flow lines), can generally be considered representative of the final fibres distribution in the section. It can be appreciated how the inclination of the flow lines along the height is changing due to the changes in the mould geometry, as the left foot is being filled.

The flow lines results are reported during the casting of section 10 in Fig. 11-a and of section 7 in Fig. 11-b. Comparing the previously obtained flow lines in section 4 (Fig. 10-b) with those in section 10 (Fig. 11-a), it can be concluded that the filling process of the foots of the tunnel lining segment can be considered symmetric and thus the obtained fibres distribution will be specular. The experimental observation introduced in the following will confirm this fact.

Additionally, it is interesting to observe the flow line distribution at the key of the tunnel lining arch, i.e., at section 7. Since the two side walls have already been filled, the casting process of the key will resemble that of a rectilinear beam, with the material flowing from one side. As also confirmed by [32,33] the outcome will be of fibres oriented almost horizontally.

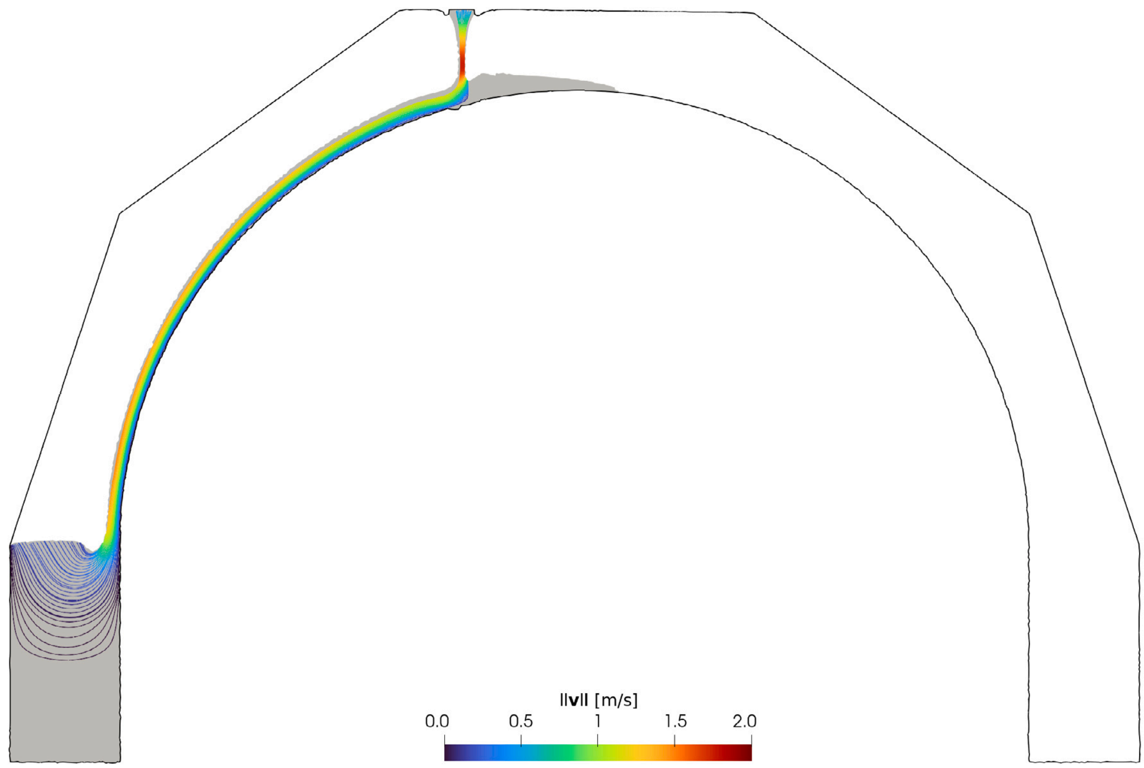

(a) Section 2, t=17.7 s

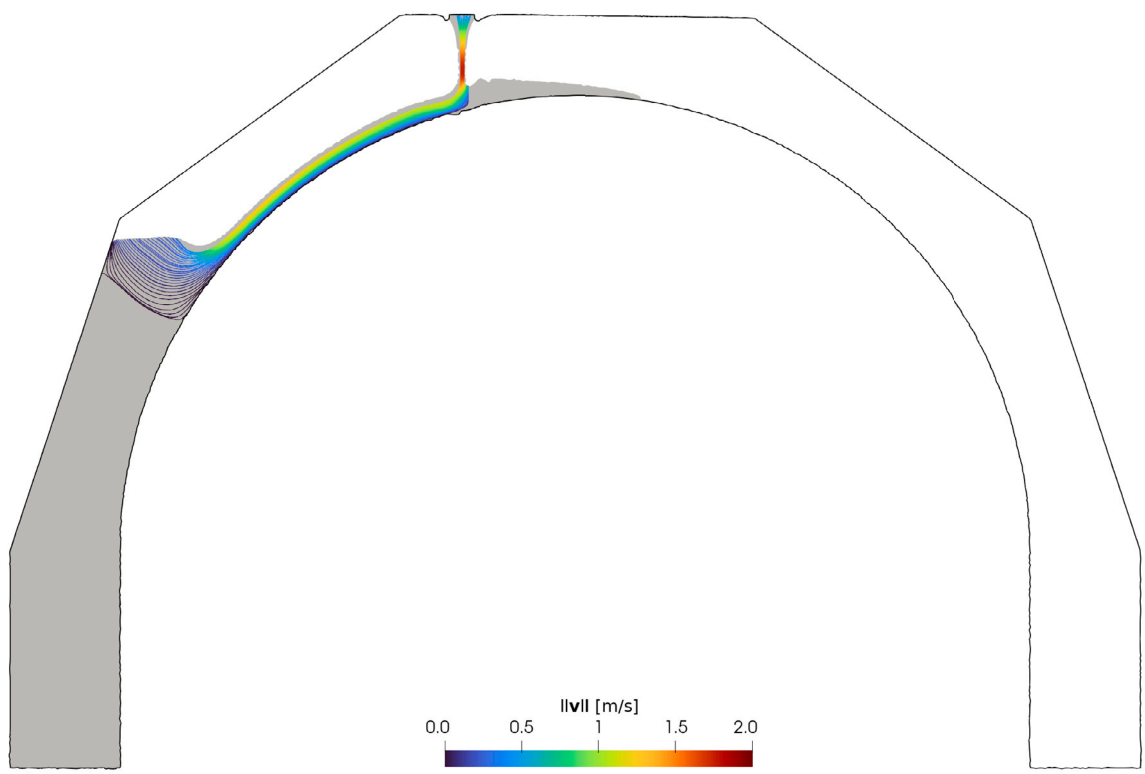

(b) Section 4, t=28.4 s

Fig. 10. Flow curves with velocity magnitude corresponding to the filling of section 2 (a) and section 4 (b).

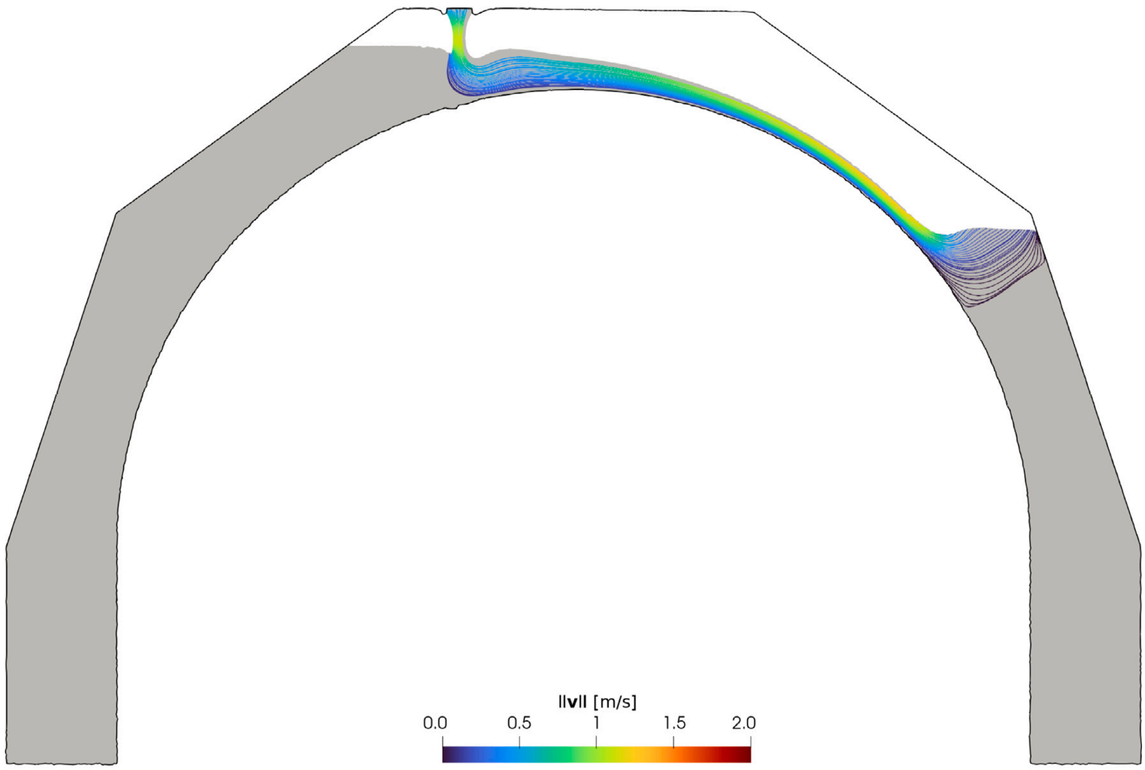

(a) Section 10, t=68.5 s

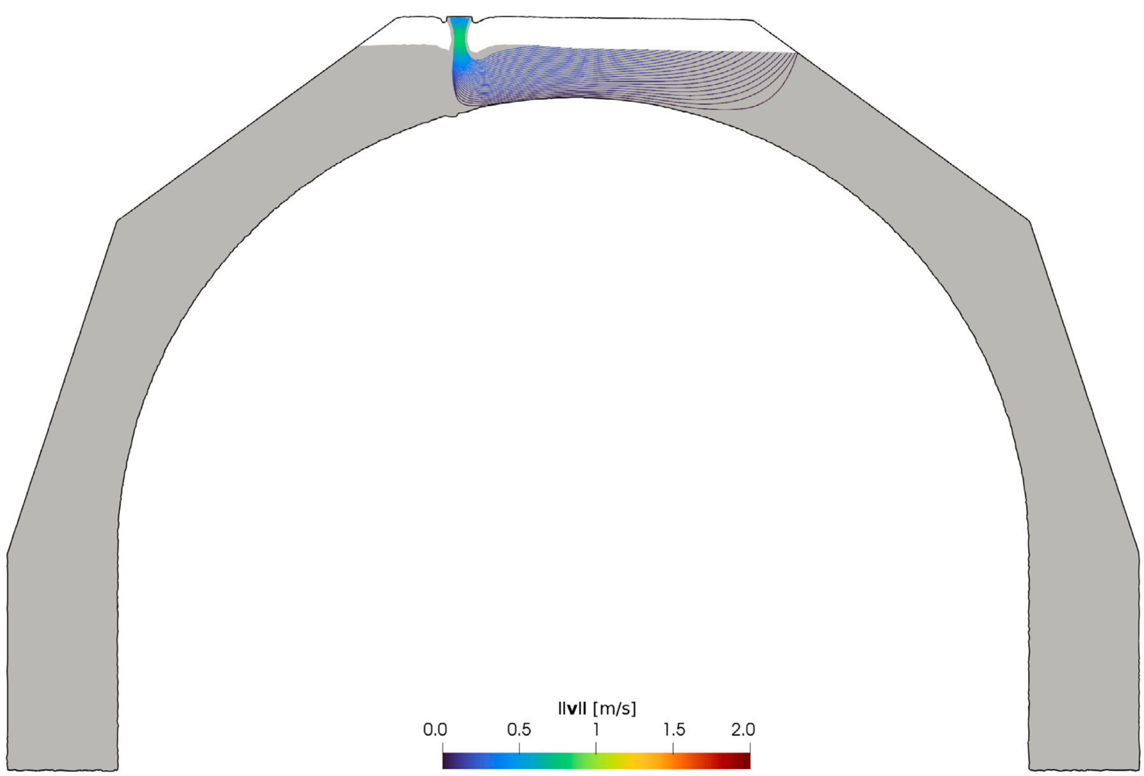

(b) Section 7, t=80.8 s

Fig. 11. Flow curves with velocity magnitude corresponding to the filling of section 10 (a) and section 7 (b).

Finally, once the flow lines corresponding to the threshold velocity have been determined for all thirteen sections under consideration (presented previously in Fig. 8), the results can be post-processed to compute the orientation factor. According to the *fib* Model Code 2010 [15], there is no single definitive method for determining the orientation factor. Various approaches have been developed, typically designed to complement either destructive or non-destructive monitoring techniques, as detailed in [19].

However, to the authors' knowledge, existing literature does not provide guidance on how to compute the orientation factor using velocity field data extracted from CFD simulations. To address this gap, a novel definition of the orientation factor is proposed, leveraging the knowledge of the flow lines. In particular, the orientation factor, hereafter denoted with k_α, can be computed as:

$$k_\alpha = \frac{\int_0^L v_n(s) \cdot ds}{\int_0^L v(s) \cdot ds}, \tag{14}$$

where a linear coordinate system s has been introduced spanning the section of total length L, as represented in Fig. 12. Moreover, $v(s) = \|\boldsymbol{v}(s)\|_2 = \sqrt{\boldsymbol{v}(s) \cdot \boldsymbol{v}(s)}$ is the L_2-norm of the velocity and $v_n(s) = |\boldsymbol{v}(s) \cdot \boldsymbol{n}|$ is the velocity projection on the section's normal.

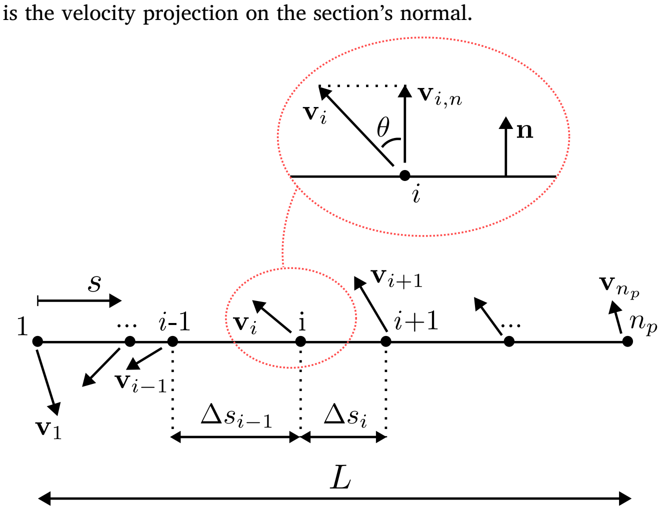

Fig. 12. Discretization of a generic section into a finite set of points, with representation of key quantities of interest such as velocity, normal velocity, and the angle between them.

Considering a generic scalar function $f(s)$ whose values can be computed at discrete points on the considered section, e.g., $f = v(s)$ or $f = v_n(s)$, the integrals can be evaluated in a simplified approximate way as:

$$\int_0^L f(s) \cdot ds \simeq f(1)\frac{\Delta s_1}{2} + \sum_{i=2}^{n_p-1} f(i)\frac{(\Delta s_{i-1} + \Delta s_i)}{2} + f(n_p)\frac{\Delta s_{n_p-1}}{2}, \tag{15}$$

where $\Delta s_i = s_{i+1} - s_i$ is the distance on the section between two consequent points. Applying the procedure introduced above, the orientation factor k_α can be computed in each section at every time, as the ratio between the integral over the section of the scalar normal velocity and the integral over the section of the scalar magnitude velocity, where both integrals can be numerically evaluated as in Eq. (15).

Fig. 13 shows the evolution of the orientation factor in time in correspondence of sections 1, 3, 5, 6, 7 and 8. The initial time considered corresponds to a situation in which the section is still characterized by a transient laminar flow, with all the material just passing through and thus associated to a $k_\alpha = 1$. Therefore, the period of interest begins just after that, at the time t_i when the section starts to being filled with concrete, and fibres start accumulating within it. The final time t_f is then defined as the moment when the average velocity $\|\bar{v}\|$ decreases below the threshold value u_{tol}. Beyond this point, further analysis of the orientation factor becomes impractical, as flow lines can no longer be accurately computed. For each section the relevant time span, identified as the period in between t_i and t_f, is highlighted in grey in Fig. 13.

Sections 1, 3 and 5 pertain to the left foot and the evolution of the orientation factor is very similar to that obtained for the corresponding symmetric sections 9, 11, 13 on the right foot. These sections are characterized by fast and moderately turbulent filling processes. Differently, longer times and smoother filling processes are associated to the sections near the key, with the exception for section 6, which is resenting of its position near the filling opening.

Although the relevant time span may vary for each section, the orientation factor always tends to decrease. This reflects the tendency of fibres to diverge from the initial flow direction (normal to the section) during the filling process. Two significant values are considered: the first is the minimum orientation factor, corresponding to the threshold velocity, and the second is the average k_α-factor over the relevant time span. The average is used instead of the maximum because the maximum typically occurs during the transient phase, when the section has just started filling.

From these values extracted for each section (average and minimum), it is possible to construct an envelope plot for the k_α-factor. This helps provide an indicative understanding of fibre orientation in each section. Specifically, the minimum value represents the most unfavourable estimate and serves as a lower bound, while the average value offers an indicative upper bound.

A non-destructive experimental campaign was performed to measure the real fibres distribution on four tunnel lining mock-ups casted in the framework of the ETLR project. The survey method is based on the use of a magnetic sensor, that, when leaned against a SFRC structure, can measure its inductance, which has been proved to be related to both the fibres content and alignment with respect to the magnetic field flow lines [18,24].

The measurements have been taken for the four tunnel linings at mid-depth, both at the intrados, extrados and side face, in correspondence of the thirteen sections under study; at each section measures were taken at four different magnet inclinations with respect to the circumferential direction: 0°, 45°, 90°, 135°. A single inclination measure with respect to the section normal has been obtained by taking a weighted average between the angles, using as weights the associated inductance values, at each section. Results are reported in Fig. 14-a,b,c. Furthermore, to provide more consistent results, the inclination value computed at each section for each mock-up has been averaged with the values obtained from the other tunnel lining mock-ups, as shown in Fig. 14-d.

The decision to study the problem under a 2D plane strain assumption is justified by the fact that the tunnel segment geometry remains nearly constant along its depth. As a result, the flow development, and consequently the fibre distribution, can also be assumed to remain fairly uniform in the out-of-plane direction.

It is worth noting that minor variations in fibre orientation may still occur, as a two-dimensional model inherently neglects three-dimensional boundary effects. These are particularly relevant at the top near the circular inlet opening and in the proximity of the two side faces, where the presence of the mould may influence local flow behaviour. Nonetheless, such effects are limited and have a negligible impact on the overall fibre distribution.

This assumption is further supported by the results shown in Fig. 14-d, which reveal similar trends in the orientation factor at the intrados, extrados, and side face. These findings indicate that three-dimensional effects are moderate, thereby validating the use of a 2D numerical model.

The computed inclination angles at each section can also be transformed into orientation factors, by considering the absolute value of their cosine. Fig. 15-a,b,c compares the experimentally measured

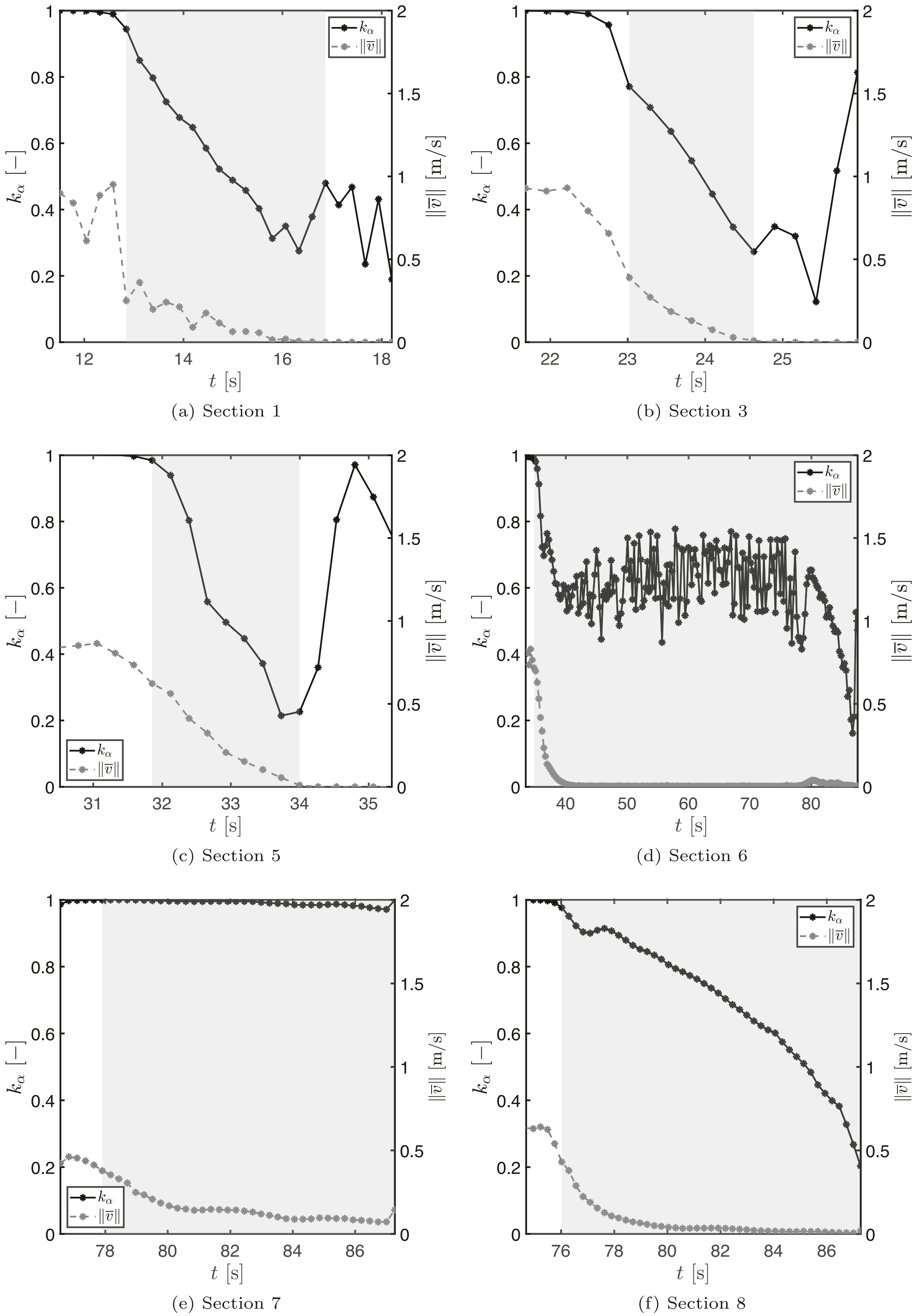

Fig. 13. Orientation factor evolution over the relevant time span (in grey) in section 1, 3, 5, 6, 7 and 8.

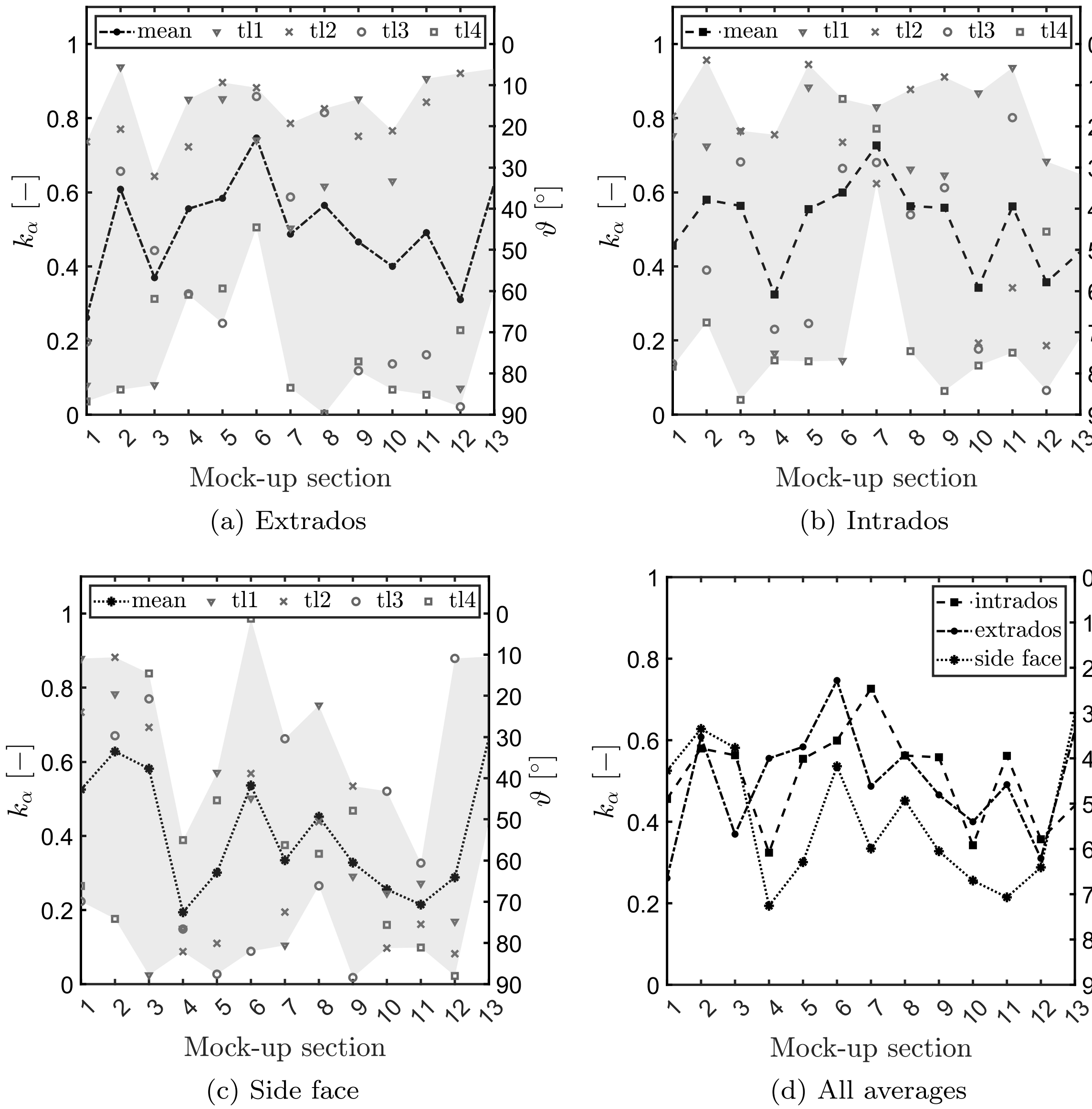

Fig. 14. Fibres inclination and orientation factor distribution at the extrados (a), intrados (b) and side face (c). Single data measures from the four tunnel linings (tl1, tl2, tl3, tl4) analysed and the mean curves (d) are reported.

averaged fibres inclination angles (and orientation factors) with the previously obtained numerical envelopes, at the extrados, intrados and side face. Finally, the intrados, extrados and revside face experimental fibres orientations can be averaged between them to obtain a more global indication of the orientation factor at a certain section of the tunnel lining, as it is reported in Fig. 15-d.

A remarkable agreement between the spatial trend of the numerically-computed orientation factor envelope and the experimentally measured data is found. The plot can be read either in terms of the orientation factor, which is useful for design purposes or in terms of the fibre orientation angle, which is the angle the fibres make with respect to the normal to the section. Both the numerical and the experimental results show a certain symmetry with respect to section 7, corresponding to the key, thus reflecting the fact that the filling process of the two side walls is similar. Also, the general trend is the same, with higher orientation factors in key, due to the more laminar filling process, resembling that of an horizontally-casted beam and with lower ones along the side walls, where turbulent filling and more mixing has occurred.

The numerical envelope not only provides a general overview of fibre orientation along the geometry, but as already stated, can also be used to draw a preliminary information on the orientation factors that, according to the *fib* Model Code 2010 [15] and 2020 [16], should be considered to perform the structural design of the investigated tunnel lining. Interestingly enough, it appears from Fig. 15 that almost all the experimental values are placed above the lower bound curve of the numerically computed envelope. Thus the numerical approach can be efficiently exploited for a safe-based design. Additionally, by examining the conclusive plot (Fig. 15-d), which represents the average experimentally-derived orientation factor across the intrados, extrados, and side face sections of the mock-up, an overall indication of the fibre alignment can be obtained. It can also be observed that nearly all of the experimental data points lie within the defined numerical envelope, and a significant portion is positioned closer to the upper bound, highlighting the reliability of the experimental measurements and at the same time providing confidence in the predictive capability of the model.

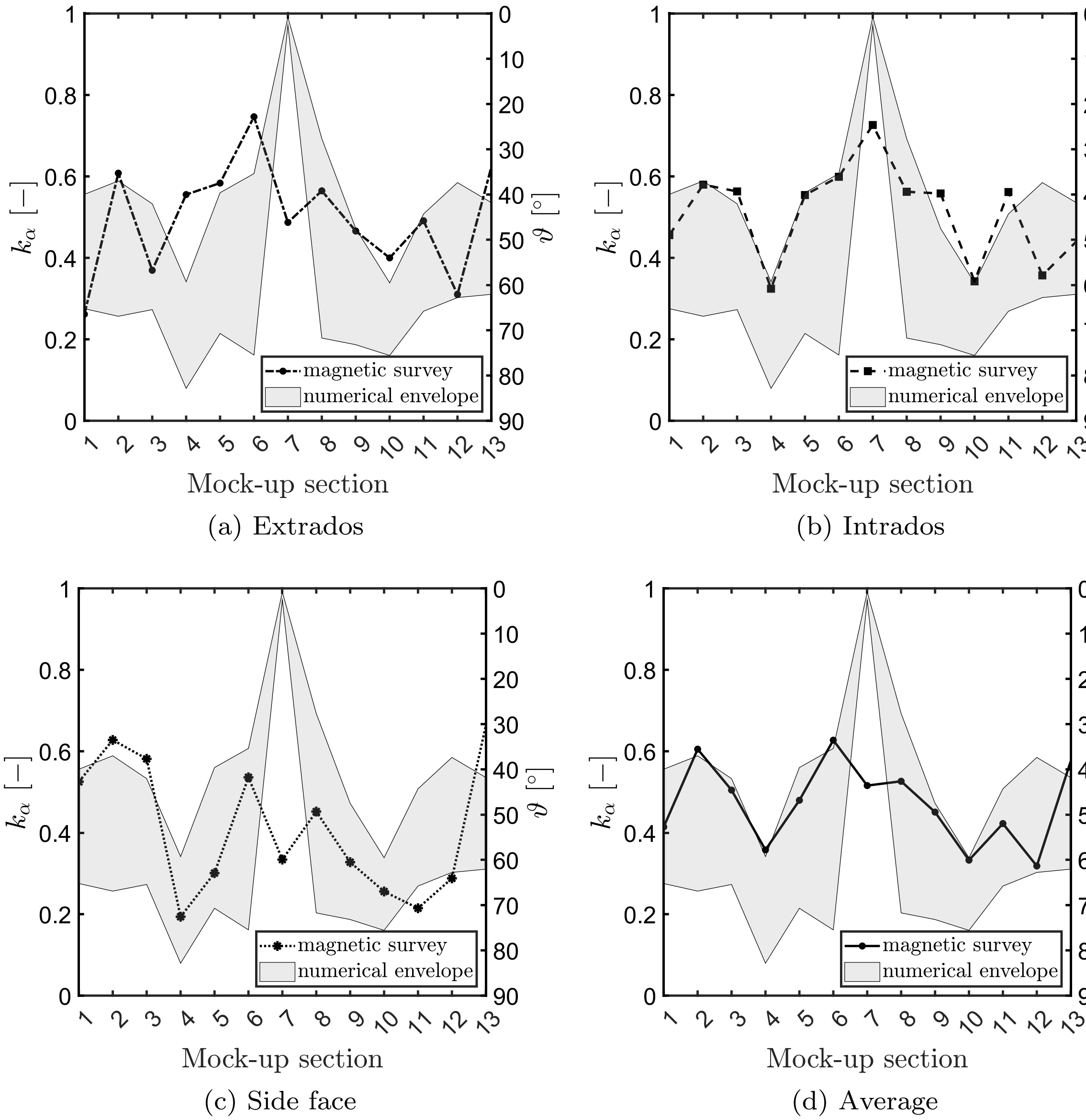

Fig. 15. Orientation factor (or equivalently fibres inclination with the section's normal) numerical envelope and experimental mean curves at the extrados (a), intrados (b), side face (c) and the average between them (d).

5. Conclusions

This study has introduced a novel and practical framework for predicting the fibre orientations in Fibre-Reinforced Self-Compacting Concrete (FR-SCC) during complex casting processes, with a particular focus on the application related to an advanced tunnel lining refurbishment technology. The methodology combines rheological characterization with fluid FEM advanced numerical modelling tecniques.

More in detail, the effect of fibres on the rheology of the investigated cementitious mixes was established by means of ICAR rheometer tests. This allowed the identification of the equivalent static yield stress and viscosity and also of their time-evolution. Notably, it was found that the presence of fibres can greatly affect thixotropic phenomena and can substantially accelerate non-reversible structuration.

The rheological data was used to calibrate a time-dependent Bingham model, to be used in the fluid FEM simulations. The latter, were performed with the Particle Finite Element Method (PFEM), a powerful technique which easily allows the simulation of complex processes involving free-surfaces and expanding domains. The model was used to simulate the entire filling process of the tunnel segment, providing an accurate evaluation of the velocity field at the different times. From post-processing operation the flow curves, representative of the fibres distribution, were generated.

Structural codes for the design of FRC elements require the computation of the orientation factor. To address this need, a novel definition of the orientation factor is introduced, relying solely on the knowledge of the velocity field. The key advantage of this approach is that the velocity field is a standard output in all CFD computational software, making the proposed procedure both general and straightforward to implement.

Finally, the experimental data from a magnetic survey campaign on cast tunnel lining segments was used to validate the numerical predictions. The measured fibre orientations closely matched those predicted by the model, confirming the reliability of both the numerical method and the novel orientation factor definition.

The results demonstrated that the developed methodology is effective for assessing fibre orientation in FR-SCC castings and can be extended to other structural applications. It can be straightforwardly applied for a design-wise evaluation of the orientation factor, as required by the structural codes. The advantages regarding structural design aspects will be further explored for the case of tunnel linings in a subsequent publication. Additionally, it can also provide multiple insights over the casting process itself, suggesting how to further optimize it to achieve an improved fibres and material distribution.

Future research could extend this methodology by incorporating two-way coupling approaches, particularly in cases where the fibre volume fraction has a significant influence on flow dynamics, an effect that the current approach does not fully capture. Another limitation arises in problems characterized by highly three-dimensional flows, where full 3D simulations are required. At present, the numerical approach is constrained by computational cost. Nevertheless, we believe that with further optimization of the numerical model, and potentially through the use of advanced CPU/GPU parallelization techniques, the methodology could already be applied to predict fibre distribution from flow in more complex geometries and even in large-scale industrial settings.

CRediT authorship contribution statement

Giacomo Rizzieri: Writing – review & editing, Writing – original draft, Visualization, Software, Methodology, Data curation, Conceptualization. **Andrea Marcucci:** Writing – review & editing, Visualization, Methodology, Data curation, Conceptualization. **Stefano Guanziroli:** Writing – review & editing, Resources, Funding acquisition. **Massimiliano Cremonesi:** Writing – review & editing, Supervision, Software, Funding acquisition. **Liberato Ferrara:** Writing – review & editing, Supervision, Methodology, Funding acquisition.

Declaration of competing interest

The authors declare that they have no known competing financial interests or personal relationships that could have appeared to influence the work reported in this paper.

Acknowledgements

The first and last author acknowledge the support of the MUSA – Multilayered Urban Sustainability Action - project, funded by the European Union – NextGenerationEU, under the National Recovery and Resilience Plan (NRRP) Mission 4 Component 2 Investment Line 1.5: Strenghtening of research structures and creation of R&D "innovation ecosystems", set up of "territorial leaders in R&D". The second and last author acknowledges the support of the Italian National Program PON Ricerca e Innovazione. This research was also partially supported by the Italian Ministry of University and Research through the project PRIN2022 DTWIX: development of Digital TWIns for multiphysics simulation of eXtreme events in civil engineering (PRIN DTWIX - 2022AL5MSN). The full scale mock-ups investigated in this study have been casted for further mechanical testing in the framework of the User Access Proiect ETLR, submitted under the call for expression of interest 2021-1-RD-ELSA-ReactionWall and shortlisted and selected by JRC Ispra.

Data availability

Data will be made available on request.

References

[1] K.H. Khayat, G. De Schutter Editors (Eds.), Mechanical Properties of Self-Compacting Concrete, vol. 14, 2014, http://dx.doi.org/10.1007/978-3-319-03245-0.

[2] N. Roussel, A thixotropy model for fresh fluid concretes: Theory, validation and applications, Cem. Concr. Res. 36 (10) (2006) 1797–1806, http://dx.doi.org/10.1016/j.cemconres.2006.05.025.

[3] N. Roussel, C. Stefani, R. Leroy, From mini-cone test to Abrams cone test: Measurement of cement-based materials yield stress using slump tests, Cem. Concr. Res. 35 (5) (2005) 817–822, http://dx.doi.org/10.1016/j.cemconres.2004.07.032.

[4] Y. Kurokawa, Y. Tanigawa, H. Mori, R. Komura, A study on the slump test and slump-flow test of fresh concrete, Trans. Jpn. Concr. Inst. 219 (8) (1994) 105–129.

[5] N. Tregger, A. Gregori, L. Ferrara, S. Shah, Correlating dynamic segregation of self-consolidating concrete to the slump-flow test, Constr. Build. Mater. 28 (1) (2012) 499–505, http://dx.doi.org/10.1016/j.conbuildmat.2011.08.052.

[6] P. Bartos, M. Sonebi, A. Tamimi, Workability and Rheology of Fresh Concrete: Compendium of Tests, RILEM Publications, Cachan, France, 2002, p. 156.

[7] M.G. Alberti, A. Enfedaque, J.C. Gálvez, The effect of fibres in the rheology of self-compacting concrete, Constr. Build. Mater. 219 (2019) 144–153, http://dx.doi.org/10.1016/j.conbuildmat.2019.05.173.

[8] E.C. Bingham, Fluidity and Plasticity, Mcgraw-Hill Book Company, Inc., New York, 1922.

[9] C.F. Ferraris, Measurement of the rheological properties of high performance concrete: State of the art report, J. Res. Natl. Inst. Stand. Technol. 104 (5) (1999) 461.

[10] N. Roussel, M. Geiker, F. Dufour, L.N. Thrane, P. Szabo, Computational modeling of concrete flow: General overview, Cem. Concr. Res. 37 (9) (2007) 1298–1307, http://dx.doi.org/10.1016/j.cemconres.2007.06.007.

[11] A. Perrot, S. Amziane, Concrete Rheometers, in: D. Sonebi Mohammedand Feys (Ed.), Measuring Rheological Properties of Cement-Based Materials: State-of-the-Art Report of the RILEM Technical Committee 266-MRP, Springer Nature Switzerland, Cham, 2024, pp. 33–71, http://dx.doi.org/10.1007/978-3-031-36743-4_3.

[12] S.P. Shah, L. Ferrara, S.H. Kwon, Recent research on self-consolidating steel fiber-reinforced concrete, in: SP-272: Antoine E. Naaman Symposium - Four Decades of Progress in Prestressed Concrete, FRC, and Thin Laminate Composite, 2010.

[13] L. Ferrara, N. Ozyurt, M. Di Prisco, High mechanical performance of fibre reinforced cementitious composites: The role of "casting-flow induced" fibre orientation, Mater. Struct. 44 (1) (2011) 109–128, http://dx.doi.org/10.1617/s11527-010-9613-9.

[14] L. Ferrara, Y.-D. Park, S.P. Shah, Correlation among fresh state behavior, fiber dispersion, and toughness properties of SFRCs, J. Mater. Civ. Eng. 20 (7) (2008) 493–501, http://dx.doi.org/10.1061/(ASCE)0899-1561(2008)20:7(493).

[15] Fédération Internationale du Béton (fib), Lausanne, Switzerland, Fib MC2010. Model Code for Concrete Structures 2010, Wilhelm Ernst & Sohn, Berlin, 2013, http://dx.doi.org/10.1002/9783433604090.

[16] Fédération Internationale du Béton (fib), Lausanne, Switzerland, Fib MC2020. Model Code for Concrete Structures 2020, 2023.

[17] A.M. Brandt, On the optimal direction of short metal fibres in brittle matrix composites, J. Mater. Sci. 20 (11) (1985) 3831–3841, http://dx.doi.org/10.1007/BF00552371.

[18] L. Ferrara, M. Faifer, M. Muhaxheri, S. Toscani, A magnetic method for non destructive monitoring of fiber dispersion and orientation in steel fiber reinforced cementitious composites. Part 2: Correlation to tensile fracture toughness, Mater. Struct. 45 (4) (2012) 591–598, http://dx.doi.org/10.1617/s11527-011-9794-x.

[19] F. Medeghini, G. Tiberti, J. Guhathakurta, S. Simon, G.A. Plizzari, P. Mark, Fiber orientation and orientation factors in steel fiber-reinforced concrete beams with hybrid fibers: A critical review, Struct. Concr. (2024) suco.202400461, http://dx.doi.org/10.1002/suco.202400461.

[20] L. Vandewalle, G. Heirman, F. Van Rickstal, Fibre orientation in self-compacting fibre reinforced concrete, in: Proceedings of the 7th International RILEM Symposium on Fibre Reinforced Concrete: Design and Applications, BEFIB 2008, RILEM Publications SARL, Bagneux, France, 2008, pp. 137–146.

[21] L. Ferrara, A. Caverzan, M. Muhaxheri, M. di Prisco, Identification of tensile behaviour of SFR-SCC: Direct vs. Indirect tests, in: J. A.O. Barros (Ed.), 8th RILEM International Symposium on Fiber Reinforced Concrete: Challenges and Opportunities, BEFIB 2012, RILEM Publications SARL, Guimarães, Portugal, 2012, pp. 209–221.

[22] M.C. Torrijos, B.E. Barragán, R.L. Zerbino, Placing conditions, mesostructural characteristics and post-cracking response of fibre reinforced self-compacting concretes, Constr. Build. Mater. 24 (6) (2010) 1078–1085, http://dx.doi.org/10.1016/j.conbuildmat.2009.11.008.

[23] L.Y. Woo, S. Wansom, N. Ozyurt, B. Mu, S.P. Shah, T.O. Mason, Characterizing fiber dispersion in cement composites using AC-Impedance Spectroscopy, Cem. Concr. Compos. 27 (6) (2005) 627–636, http://dx.doi.org/10.1016/j.cemconcomp.2004.06.003.

[24] L. Ferrara, M. Faifer, S. Toscani, A magnetic method for non destructive monitoring of fiber dispersion and orientation in steel fiber reinforced cementitious composites—Part 1: Method calibration, Mater. Struct. 45 (4) (2012) 575–589, http://dx.doi.org/10.1617/s11527-011-9793-y.

[25] P. Stähli, R. Custer, J.G.M. Van Mier, On flow properties, fibre distribution, fibre orientation and flexural behaviour of FRC, Mater. Struct. 41 (1) (2008) 189–196, http://dx.doi.org/10.1617/s11527-007-9229-x.

[26] L. Martinie, N. Roussel, Simple tools for fiber orientation prediction in industrial practice, Cem. Concr. Res. 41 (10) (2011) 993–1000, http://dx.doi.org/10.1016/j.cemconres.2011.05.008.

[27] N. Roussel, J. Spangenberg, J. Wallevik, R. Wolfs, Numerical simulations of concrete processing: From standard formative casting to additive manufacturing, Cem. Concr. Res. 135 (2020) http://dx.doi.org/10.1016/j.cemconres.2020.106075.

[28] F. Folgar, Charles.L. Tucker III, Orientation behavior of fibers in concentrated suspensions, J. Reinf. Plast. Compos. 3 (2) (1984) 98–119, http://dx.doi.org/10.1177/073168448400300201.

[29] S.G. Advani, Charles.L. Tucker III, The use of tensors to describe and predict fiber orientation in short fiber composites, J. Rheol. 31 (8) (1987) 751–784, http://dx.doi.org/10.1122/1.549945.

[30] F. Kolařík, B. Patzák, L.N. Thrane, Modeling of fiber orientation in viscous fluid flow with application to self-compacting concrete, Comput. Struct. 154 (2015) 91–100, http://dx.doi.org/10.1016/j.compstruc.2015.03.007.

[31] V. Gudžulić, T.S. Dang, G. Meschke, Computational modeling of fiber flow during casting of fresh concrete, Comput. Mech. 63 (6) (2019) 1111–1129, http://dx.doi.org/10.1007/s00466-018-1639-9.

[32] L. Ferrara, M. Cremonesi, Effects of casting process on toughness properties of Fiber Reinforced- Self Compacting Concrete as from EN 1465, in: Rheology and Processing of Construction Materials, 2013.

[33] L. Ferrara, M. Cremonesi, M. Faifer, S. Toscani, L. Sorelli, M.A. Baril, J. Réthoré, F. Baby, F. Toutlemonde, S. Bernardi, Structural elements made with highly flowable UHPFRC: Correlating computational fluid dynamics (CFD) predictions and non-destructive survey of fiber dispersion with failure modes, Eng. Struct. 133 (2017) 151–171, http://dx.doi.org/10.1016/j.engstruct.2016.12.026.

[34] V. Mechtcherine, A. Gram, K. Krenzer, J.H. Schwabe, S. Shyshko, N. Roussel, Simulation of fresh concrete flow using Discrete Element Method (DEM): Theory and applications, Mater. Struct. 47 (4) (2014) 615–630, http://dx.doi.org/10.1617/s11527-013-0084-7.

[35] Y. Zhao, J. Bi, L. Huo, Z. Wang, J. Guan, Y. Zhao, Development of a coupled numerical framework of steel fiber reinforced self-compacting concrete, Constr. Build. Mater. 303 (2021) 124582, http://dx.doi.org/10.1016/j.conbuildmat.2021.124582.

[36] S. Guanziroli, A. Marcucci, A. Negrini, L. Ferrara, B. Chiaia, A new concept of additive manufacturing for the regeneration of existing tunnels, in: M.A. Aiello, A. Bilotta (Eds.), Proceedings of Italian Concrete Conference 2022, 2024, pp. 116–124, http://dx.doi.org/10.1007/978-3-031-43102-9_10.

[37] E. Oñate, S.R. Idelsohn, F. Del Pin, R. Aubry, The particle finite element method. An overview, Int. J. Comput. Methods 1 (2) (2004) 267–307, http://dx.doi.org/10.1142/S0219876204000204.

[38] M. Cremonesi, A. Franci, S. Idelsohn, E. Oñate, A state of the art review of the particle finite element method (PFEM), Arch. Comput. Methods Eng. 27 (5) (2020) 1709–1735, http://dx.doi.org/10.1007/s11831-020-09468-4.

[39] L. Martinie, P. Rossi, N. Roussel, Rheology of fiber reinforced cementitious materials: Classification and prediction, Cem. Concr. Res. 40 (2) (2010) 226–234, http://dx.doi.org/10.1016/j.cemconres.2009.08.032.

[40] ICAR plus concrete rheometer manual.

[41] M. Reiner, H. Eyring, Deformation and flow. An elementary introduction to theoretical rheology, Phys. Today 3 (4) (1950) 35–36, http://dx.doi.org/10.1063/1.3066868.

[42] D. Feys, J.E. Wallevik, A. Yahia, K.H. Khayat, O.H. Wallevik, Extension of the Reiner-Riwlin equation to determine modified Bingham parameters measured in coaxial cylinders rheometers, Mater. Struct./Mater. Constr 46 (1–2) (2013) 289–311, http://dx.doi.org/10.1617/s11527-012-9902-6.

[43] J.T. Kolawole, R. Combrinck, W.P. Boshoff, Measuring the thixotropy of conventional concrete: The influence of viscosity modifying agent, superplasticiser and water, Constr. Build. Mater. 225 (2019) 853–867, http://dx.doi.org/10.1016/j.conbuildmat.2019.07.240.

[44] N. Roussel, G. Ovarlez, S. Garrault, C. Brumaud, The origins of thixotropy of fresh cement pastes, Cem. Concr. Res. 42 (1) (2012) 148–157, http://dx.doi.org/10.1016/j.cemconres.2011.09.004.

[45] J.E. Wallevik, Rheological properties of cement paste: Thixotropic behavior and structural breakdown, Cem. Concr. Res. 39 (1) (2009) 14–29, http://dx.doi.org/10.1016/j.cemconres.2008.10.001.

[46] O.H. Wallevik, D. Feys, J.E. Wallevik, K.H. Khayat, Avoiding inaccurate interpretations of rheological measurements for cement-based materials, Cem. Concr. Res. 78 (2015) 100–109, http://dx.doi.org/10.1016/j.cemconres.2015.05.003.

[47] G. Krage, O.H. Wallevik, Rheology of synthetic-fiber reinforced SCC, in: 5th International RILEM Symposium on Self-Compacting Concrete, Ghent, Belgium, 2007.

[48] M. Cremonesi, L. Ferrara, A. Frangi, U. Perego, Simulation of the flow of fresh cement suspensions by a Lagrangian finite element approach, J. Non-Newton. Fluid Mech. 165 (23–24) (2010) 1555–1563, http://dx.doi.org/10.1016/j.jnnfm.2010.08.003.

[49] G. Rizzieri, L. Ferrara, M. Cremonesi, Numerical simulation of the extrusion and layer deposition processes in 3D concrete printing with the Particle Finite Element Method, Comput. Mech. (2023) http://dx.doi.org/10.1007/s00466-023-02367-y.

[50] G. Rizzieri, M. Cremonesi, L. Ferrara, A 2D numerical model of 3D concrete printing including thixotropy, Mater. Today (2023) http://dx.doi.org/10.1016/j.matpr.2023.08.082.

[51] G. Rizzieri, S. Meni, M. Cremonesi, L. Ferrara, A Particle Finite Element Method for investigating the influence of material and process parameters in 3D Concrete Printing, Comput. Struct. 316 (2025) 107883, http://dx.doi.org/10.1016/j.compstruc.2025.107883.

[52] H.-W. Reinhardt, C. Grosse, B. Weiler, J. Bohnert, N. Windisch, P-wave propagation in setting and hardening concrete, Otto-Graf-J. 7 (1996) 181–189.

[53] T.C. Papanastasiou, Flows of materials with yield, J. Rheol. 31 (5) (1987) 385–404, http://dx.doi.org/10.1122/1.549926.

[54] G. Rizzieri, L. Ferrara, M. Cremonesi, A partitioned Lagrangian finite element approach for the simulation of viscoelastic and elasto-viscoplastic free-surface flows, Comput. Methods Appl. Mech. Engrg. 443 (2025) 118071, http://dx.doi.org/10.1016/j.cma.2025.118071.

[55] T.J.R. Hughes, L.P. Franca, M. Balestra, A new finite element formulation for computational fluid dynamics: V. Circumventing the Babuška-Brezzi condition: A stable Petrov-Galerkin formulation of the Stokes problem accommodating equal-order interpolations, Comput. Methods Appl. Mech. Engrg. 59 (1) (1986) 85–99, http://dx.doi.org/10.1016/0045-7825(86)90025-3.

[56] S.R. Idelsohn, E. Oñate, F. Del Pin, The particle finite element method: A powerful tool to solve incompressible flows with free-surfaces and breaking waves, Int. J. Comput. Methods 61 (7) (2004) 964–989, http://dx.doi.org/10.1002/nme.1096.

[57] G. Rizzieri, M. Cremonesi, L. Ferrara, Challenging the limits of fluid FEM modelling in 3D concrete printing, in: D. Lowke, N. Freund, D. Böhler, F. Herding (Eds.), Fourth RILEM International Conference on Concrete and Digital Fabrication. DC 2024, Springer Nature Switzerland, Cham, 2024, pp. 482–489, http://dx.doi.org/10.1007/978-3-031-70031-6_56.

[58] G. Rizzieri, L. Ferrara, M. Cremonesi, Simulation of viscoelastic free-surface flows with the Particle Finite Element Method, Comput. Part. Mech. (2024) http://dx.doi.org/10.1007/s40571-024-00730-1.

[59] H. Si, TetGen, a Delaunay-based quality tetrahedral mesh generator, ACM Trans. Math. Software 41 (2) (2015) http://dx.doi.org/10.1145/2629697.

[60] H. Edelsbrunner, E.P. Mücke, Three-dimensional alpha shapes, ACM Trans. Graph. 13 (1) (1994) 43–72, http://dx.doi.org/10.1145/174462.156635.

[61] A. Marcucci, S. Guanziroli, L. Ferrara, Additive Manufacturing for the regeneration of existing tunnels: A new slip-forming technique using FRC, in: FRC2023: Fiber Reinforced Concrete: From Design To Structural Applications, 2023.